



Effects of Porosity Distribution on the Dynamic Behavior of Two Varieties of SiC

by Samuel R. Martin

ARL-TR-3374

December 2004

NOTICES

Disclaimers

The findings in this report are not to be construed as an official Department of the Army position unless so designated by other authorized documents.

Citation of manufacturer's or trade names does not constitute an official endorsement or approval of the use thereof.

Destroy this report when it is no longer needed. Do not return it to the originator.

Army Research Laboratory

Aberdeen Proving Ground, MD 21005-5066

ARL-TR-3374**December 2004**

Effects of Porosity Distribution on the Dynamic Behavior of Two Varieties of SiC

Samuel R. Martin

Weapons and Materials Research Directorate, ARL

REPORT DOCUMENTATION PAGE			Form Approved OMB No. 0704-0188		
Public reporting burden for this collection of information is estimated to average 1 hour per response, including the time for reviewing instructions, searching existing data sources, gathering and maintaining the data needed, and completing and reviewing the collection information. Send comments regarding this burden estimate or any other aspect of this collection of information, including suggestions for reducing the burden, to Department of Defense, Washington Headquarters Services, Directorate for Information Operations and Reports (0704-0188), 1215 Jefferson Davis Highway, Suite 1204, Arlington, VA 22202-4302. Respondents should be aware that notwithstanding any other provision of law, no person shall be subject to any penalty for failing to comply with a collection of information if it does not display a currently valid OMB control number. PLEASE DO NOT RETURN YOUR FORM TO THE ABOVE ADDRESS.					
1. REPORT DATE (DD-MM-YYYY) December 2004		2. REPORT TYPE Final		3. DATES COVERED (From - To) 1 July 2003–24 May 2004	
4. TITLE AND SUBTITLE Effects of Porosity Distribution on the Dynamic Behavior of Two Varieties of SiC			5a. CONTRACT NUMBER		
			5b. GRANT NUMBER		
			5c. PROGRAM ELEMENT NUMBER		
6. AUTHOR(S) Samuel R. Martin			5d. PROJECT NUMBER 622601DC05		
			5e. TASK NUMBER		
			5f. WORK UNIT NUMBER		
7. PERFORMING ORGANIZATION NAME(S) AND ADDRESS(ES) U. S. Army Research Laboratory ATTN: AMSRD-ARL-WM-TA Aberdeen Proving Ground, MD 21005-5066			8. PERFORMING ORGANIZATION REPORT NUMBER ARL-TR-3374		
9. SPONSORING/MONITORING AGENCY NAME(S) AND ADDRESS(ES)			10. SPONSOR/MONITOR'S ACRONYM(S)		
			11. SPONSOR/MONITOR'S REPORT NUMBER(S)		
12. DISTRIBUTION/AVAILABILITY STATEMENT Approved for public release; distribution is unlimited.					
13. SUPPLEMENTARY NOTES					
14. ABSTRACT In order to understand the microstructural reasons behind variations in ballistic material properties, plate-impact tests were conducted on two sintered silicon carbides with slightly different microstructures. Regular Hexoloy (RH) and Enhanced Hexoloy (EH) were obtained from Saint-Gobain. It was determined that the porosity distribution in EH had fewer large pores leading to an 18% increase in flexural strength over that for RH. Plate-impact experiments were conducted utilizing a VISAR to measure free-surface velocities. Tests were performed on each material to determine the Hugoniot Elastic Limit (HEL) and spall strength. Spall strength was measured as a function of impact stress, and pulse duration. Results show the difference in porosity distribution between EH and RH results in no discernable difference in their HEL values and spall strengths. The spall strengths were independent of pulse width and showed a trend similar to that found in other studies for SiC. Both materials demonstrated finite spall strength above the HEL.					
15. SUBJECT TERMS dynamic behavior, SiC, plate impact, HEL, spall, fracture toughness, Hexoloy, flexure strength					
16. SECURITY CLASSIFICATION OF:			17. LIMITATION OF ABSTRACT UL	18. NUMBER OF PAGES 52	19a. NAME OF RESPONSIBLE PERSON Samuel R. Martin
a. REPORT UNCLASSIFIED	b. ABSTRACT UNCLASSIFIED	c. THIS PAGE UNCLASSIFIED			19b. TELEPHONE NUMBER (Include area code) 410-278-6081

Contents

List of Figures	v
List of Tables	vi
Acknowledgments	vii
1. Introduction and Background	1
2. Microstructural Characterization	3
2.1 Ceramic Processing Techniques.....	3
2.2 Regular Hexoloy and Enhanced Hexoloy	3
2.3 Density, Elastic Wavespeeds, and Elastic Constants	3
2.4 Microstructural Investigation	4
2.5 Determination of Grain Size and Morphology	5
2.6 Determination of Pore Size Distribution and Pore Volume Percent	7
2.7 Hardness	9
2.8 Effect of Elongated Grains on Fracture Toughness	9
2.9 Fracture Toughness	10
2.10 Flexural Strength	11
2.11 Discussion	11
3. Experimental Configurations	12
3.1 Plate-Impact Experiment.....	12
3.2 VISAR	14
3.3 Plate-Impact Specimens	15
3.4 Experimental Setup	15
3.5 Theory	17
3.6 Spall Strength	18
3.7 Identification of Spallation on an X-T Diagram	18
3.8 Estimate of Spall Strength From Free-Surface Velocity Profile	20
3.9 Experimental Configuration for Determining Spall Strength	22

3.10 Experimental Configuration for Determining Spall Strength Above HEL	22
3.11 HEL	24
4. Results	25
4.1 Spall Strength	25
4.2 HEL	31
4.3 Comparison to Other SiCs.....	33
5. Conclusions	34
6. References	36
Appendix: Specimen Preparation	39
Distribution List	40

List of Figures

Figure 1. Regular Hexoloy 500×.	4
Figure 2. Enhanced Hexoloy 500×.	4
Figure 3. Grayscale to binary (black/white) image.	5
Figure 4. Grain size frequency percent distribution.	6
Figure 5. Aspect ratio frequency percent distribution.	6
Figure 6. Regular Hexoloy 100×.	7
Figure 7. Enhanced Hexoloy 100×.	7
Figure 8. Regular Hexoloy 200×.	8
Figure 9. Enhanced Hexoloy 200×.	8
Figure 10. Pore size frequency percent distribution with blowup of larger pore sizes.	8
Figure 11. Pore size total frequency distribution with blowup of larger pore sizes.	8
Figure 12. Gas gun schematic.	13
Figure 13. Probe setup.	14
Figure 14. VISAR configuration.	15
Figure 15. Diagram of cross section of projectile and target.	16
Figure 16. Front view of flyer.	16
Figure 17. Front view of target.	17
Figure 18. X-T diagram 2-mm flyer.	19
Figure 19. X-T diagram 4-mm flyer.	19
Figure 20. Stress vs. particle velocity diagram.	21
Figure 21. Free-surface velocity vs. time diagram.	21
Figure 22. Stress vs. velocity with impedance mismatch (purely elastic response).	23
Figure 23. Stress vs. velocity using material elastic-plastic response.	23
Figure 24. Stress vs. velocity using elastic-plastic response of target and Hugoniot curve of flyer.	25
Figure 25. Spall strength vs. impact stress.	27
Figure 26. Free-surface velocity profiles of EH with 2-mm flyers.	28
Figure 27. Free-surface velocity profiles of EH with 4-mm flyers.	28
Figure 28. Free-surface velocity profiles of EH with 2- and 4-mm flyers.	29
Figure 29. Free-surface velocity profiles of RH with 2-mm flyers.	29
Figure 30. Repeatability tests, RH at ~300m/s with 2-mm flyers.	30

Figure 31. Free-surface velocity profiles of RH with 4-mm flyers.	30
Figure 32. HEL profiles for RH.	32
Figure 33. HEL profiles for EH.	32
Figure 34. Comparison to other SiCs.	33

List of Tables

Table 1. Elastic constants.	4
Table 2. Microstructural analysis data.	9
Table 3. Summary of material properties.	12
Table 4. Shot summary.	26
Table 5. Pulse widths and times to arrival of cylindrical wave.	26
Table A-1. Polishing procedure for SiC.	39
Table A-2. Preparation of plate-impact specimens.	39

Acknowledgments

I would like to thank Dr. Dattatraya Dandekar for all his advice and help concerning the plate-impact experiments. In addition, I would like to thank Drs. Min Zhou and Naresh Thadhani of the Georgia Institute of Technology for reviewing the document. I would like to thank Dr. Jerry LaSalvia for obtaining the material samples and for his advice on the materials characterization. I would also like to thank Tim Cline and Mike Blount for their assistance with the gas gun.

INTENTIONALLY LEFT BLANK.

1. Introduction and Background

For years the military has sought to use the properties of ceramics for armor applications. Current high-performance ceramics have extremely high compressive strengths and low densities. The extreme hardness values and compressive strengths of ceramics can resist penetration altogether in certain configurations. When they are penetrated, ceramics can still demonstrate very high resistance to penetration. For these reasons, ceramics have been the subjects of thorough, in-depth ballistic testing both in the field and laboratory.

Hauver et al. (1) demonstrated a new mechanism in the defeat of long-rod penetrators using ceramics. Under certain impact conditions, instead of penetrating the target, a long-rod projectile can be defeated at the surface of a ceramic. In this case, material flows radially outwards on the surface of the ceramic for the duration of the ballistic event. This process has been termed “interface defeat.” Lundberg et al. (2) looked further into this phenomenon, performing a study that looked at the velocity range where interface defeat of a long-rod penetrator transitioned to more traditional penetration behavior. The velocity where this occurs is termed the transition velocity interval. A higher transition velocity correlates to increased resistance to penetration and greater erosion of the projectile.

Numerous ceramics have been studied in the literature, including: silicon carbide (SiC), alumina (Al_2O_3), aluminum nitride (AlN), boron carbide (B_4C), and titanium diboride (TiB_2). Lundberg found SiC to have a higher transition velocity interval than TiB_2 and B_4C . Measurements of shock wave profiles have shown that SiC and TiB_2 undergo deformation-induced hardening, which may give rise to improved ballistic properties (3). B_4C shows the opposite: significant softening and loss of strength above the HEL (4). Orphal et al. (5–7) performed tests in which penetration depth vs. impact velocity was examined using a semi-infinite ceramic target configuration. They found that, under similar impact conditions and configurations, SiC demonstrated less total penetration than B_4C and AlN. Overall, SiC has presented itself as one of the more attractive options not only due to its good penetration behavior, but also because of its low density and lower cost.

In addition to performance variations from ceramic to ceramic, it has also been observed that there can be significant variations even within the same type of ceramic. Minute differences in microstructure drastically affect ceramic properties and ballistic performance. Variations in porosity, density, impurities, glassy phases, and grain morphology can have an effect. These microstructural entities are directly related to the processing techniques used to take the initial powders to the final product. The main methods are hot pressing, pressureless sintering, and reaction bonding. Each process uses different dopants to aid in sintering, remove glassy phases, isolate impurities, and assist in densification.

It is of great interest to investigate why and how microstructural properties relate to ballistic performance. The reason is threefold. First, such investigations could lead to improved armor packages by offering insight to the armor developer when selecting ceramic materials. Second, it would offer insight to the materials scientist who could, in turn, design a better armor ceramic. Lastly, material modelers could incorporate the information into computer code used in simulating dynamic events. The interest of this study is to (1) quantitatively characterize two sintered silicon carbides with slightly different microstructures, (2) study their response to dynamic loads, and (3) develop a better fundamental understanding of microstructural influences on dynamic material behavior. Several studies have been conducted where material properties of one ceramic type are varied and the dynamic behavior is tested and analyzed. Usually, from one variation to the next, several properties are different making it hard to isolate the effect of each. For this study, the only difference in the materials was porosity distribution.

Two variations of a silicon carbide with the trade name Hexoloy^{*} SA were obtained through Saint-Gobain. Regular Hexoloy (RH) and Enhanced Hexoloy (EH) are pressureless sintered products having exactly the same chemistries. EH went through additional powder processing prior to sintering, producing a final product with a slightly different morphology than RH. Samples of each were characterized microstructurally including morphology, density, elastic wavespeeds, microhardness, fracture toughness, and flexure strength. The characterization revealed differences in porosity distribution and flexure strength. It was determined that the porosity distribution in EH had fewer large pores leading to an 18% increase in flexural strength over that for RH.

Planar plate-impact experiments were used to characterize material behavior at high deformation rates and impact stresses. Typical strain rates were in excess of 10^5 and impact stresses ranged from 1 to 16 GPa. A velocity interferometer system for any reflector (VISAR) was used to obtain free-surface velocity profiles. Several dynamic, material properties are determined from these profiles. The Hugoniot Elastic Limit (HEL) was taken to be the break in the slope between the elastic and plastic rise in the free-surface velocity profile. Most authors agree that HEL is the ballistic measure of yield within the material under uniaxial strain. Spall strength is taken to be a measure of a material's dynamic tensile strength. For this study, spall strength was measured as a function of impact stress and pulse duration. The HEL and spall strength values for a particular ceramic may vary depending upon processing and microstructure. Such influences are examined in this report and are presented in this order: microstructural characterization, plate-impact testing, results, and conclusion.

^{*} Hexoloy is a registered trademark of Saint-Gobain, Niagara Falls, NY.

2. Microstructural Characterization

2.1 Ceramic Processing Techniques

The mechanical properties of SiC are presumed to be dependent on the grain size of the powder, processing temperature, sintering aids, the powder blending process, and elemental composition of the compounds present in the processed materials. Silicon carbide cannot be consolidated without sintering aids. The conventional sintering aids for consolidation of SiC powder are boron, carbon, and aluminum nitride.

Complete understandings of the roles of each microstructural detail on the impact performance in SiC are not known; therefore a material characterization was performed on the samples to be tested. Optimally, just one variation in microstructure is desired in order to differentiate with certainty what impact it has on the material's overall dynamic behavior.

2.2 Regular Hexoloy and Enhanced Hexoloy

The materials used in this study go by the trade names Hexoloy SA and Enhanced Hexoloy and are commercially manufactured by Saint-Gobain. The materials shall be abbreviated as RH for Regular Hexoloy and EH for Enhanced Hexoloy. The materials are both pressureless sintered silicon carbides of identical chemical composition. The only difference lies in their pore distributions. This is achieved by refining EH's presintered powder further with additional grinding and presintering compaction. The additional powder processing reduces the size of the largest flaw and therefore gives EH a higher flexure strength.

2.3 Density, Elastic Wavespeeds, and Elastic Constants

Density measurements were conducted using Archimedes Principle, which determines density through water displacement. American Society for Testing of Materials (ASTM) standard B311 gives a good summary of the technique used (8). The density of RH was $3.152 \pm 0.006 \text{ g/cm}^3$, and EH was $3.156 \pm 0.005 \text{ g/cm}^3$. Elastic wave speeds in the SiC were measured using non-destructive ultrasonic techniques. RH had a longitudinal and shear wave speed of $12.03 \pm 0.04 \text{ km/s}$ and $7.62 \pm 0.03 \text{ km/s}$, respectively. The EH had a longitudinal and shear wave speed of $12.13 \pm 0.01 \text{ km/s}$ and $7.64 \pm 0.02 \text{ km/s}$, respectively. The bulk wave speed, although not directly measured, was calculated to be $8.21 \pm 0.08 \text{ km/s}$ and $8.33 \pm 0.03 \text{ km/s}$, for RH and EH, respectively. Material constants were calculated from the measured densities and elastic wave speeds. See table 1 for values.

Table 1. Elastic constants.

		Regular	Enhanced
E	(GPa)	427 ± 2	432 ± 1
G	(GPa)	183 ± 2	184 ± 1
B	(GPa)	212 ± 4	219 ± 1
ν		0.165 ± 0.007	0.171 ± 0.003

2.4 Microstructural Investigation

In order to investigate the grains it was necessary to section, polish, and etch the samples. All of these processes are described in detail in appendix A. Samples were sectioned using a diamond saw and then polished. To ease polishing, the samples were mounted in Bakelite.[†] These mounted specimens were placed in an automatic polisher capable of polishing six samples at a time. After polishing, the samples were removed from the plastic holder and etched in a modified-murakami solution to dissolve the grain boundaries. Pictures were taken at 500 \times on an optical microscope. For each material, orthogonal planes were analyzed to look for anisotropy. For each specimen, five different locations were sampled. The images were calibrated to scale according to magnification lens. The images were saved with the appropriate scale bar and analysis was later done using Image-Pro Plus software. Figures 1 and 2 show the microstructures of RH and EH. No anisotropy was found.

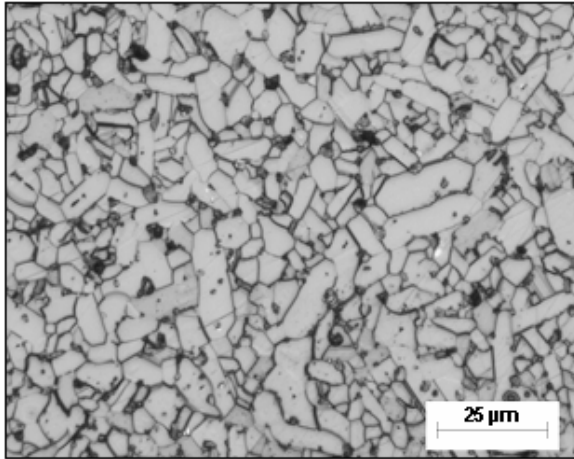


Figure 1. Regular Hexoloy 500 \times .

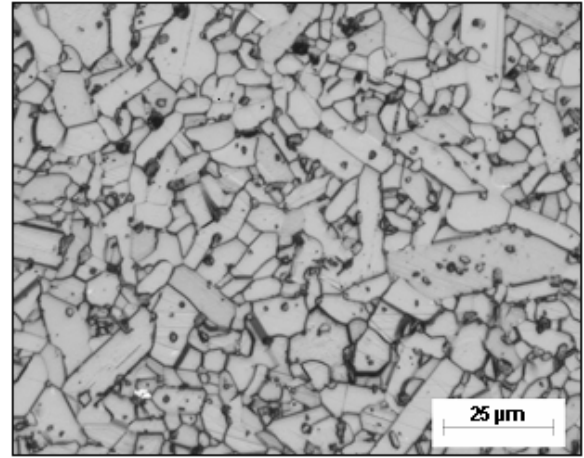


Figure 2. Enhanced Hexoloy 500 \times .

[†] Bakelite is a registered trademark of Bakelite AG, Germany.

2.5 Determination of Grain Size and Morphology

Average grain size, grain size distribution, average aspect ratio, and aspect ratio distribution were determined by converting the micrographs into black and white pictures using Adobe Photoshop. Once the binary images were produced (figure 3), they were inserted into Image-Pro Plus. The images were calibrated and the automatic counting function was used. The program automatically calculated values for grain area and aspect ratio. Grain area was calculated by counting pixels. The grain diameters were calculated from the grain area via the equation for a circle. The data from Image-Pro Plus was exported to Excel where the results were averaged and then tabulated on a frequency percent basis. For RH, four micrographs from each of the orthogonal faces were analyzed. After talking with representatives from the company and taking the amount of time needed to enhance the images into consideration, only two micrographs of EH were analyzed. There was little difference in grain size distributions between the two materials as can be seen from figure 4. Aspect ratio frequency percent distributions were obtained the same way. From figure 5 it can be seen that there is little difference in the aspect ratio distribution as well.

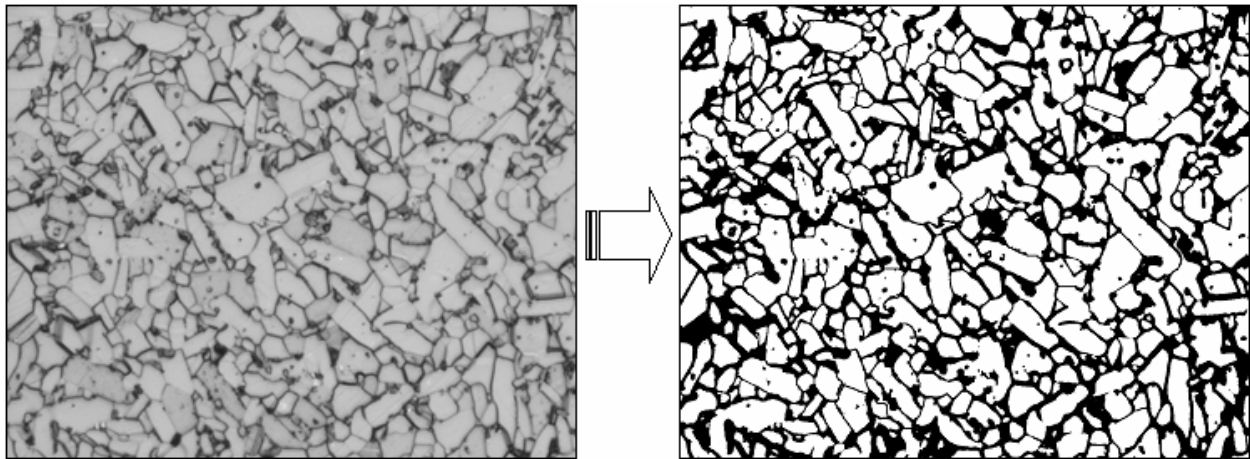


Figure 3. Grayscale to binary (black/white) image.

When looking through the microscope at a lower magnification, it was noticeable that EH had a larger number of elongated grains. This was not apparent from the grain size and aspect ratio distributions. Figures 6 and 7 show micrographs of RH and EH, respectively, at 100× magnification. The area fraction percent of elongated grains was calculated to give a more quantitative measure of the differences between the two materials. The areas of elongated grains over $1000 \mu\text{m}^2$ and with an aspect ratio of at least 8 were summed and divided by the total area of the micrograph to give area fraction percent. Ten micrographs of each material were analyzed. EH was found to have approximately 4% area fraction, where RH had close to 0%. In following sections, it will be discussed what effect the elongated grains may have on material properties.

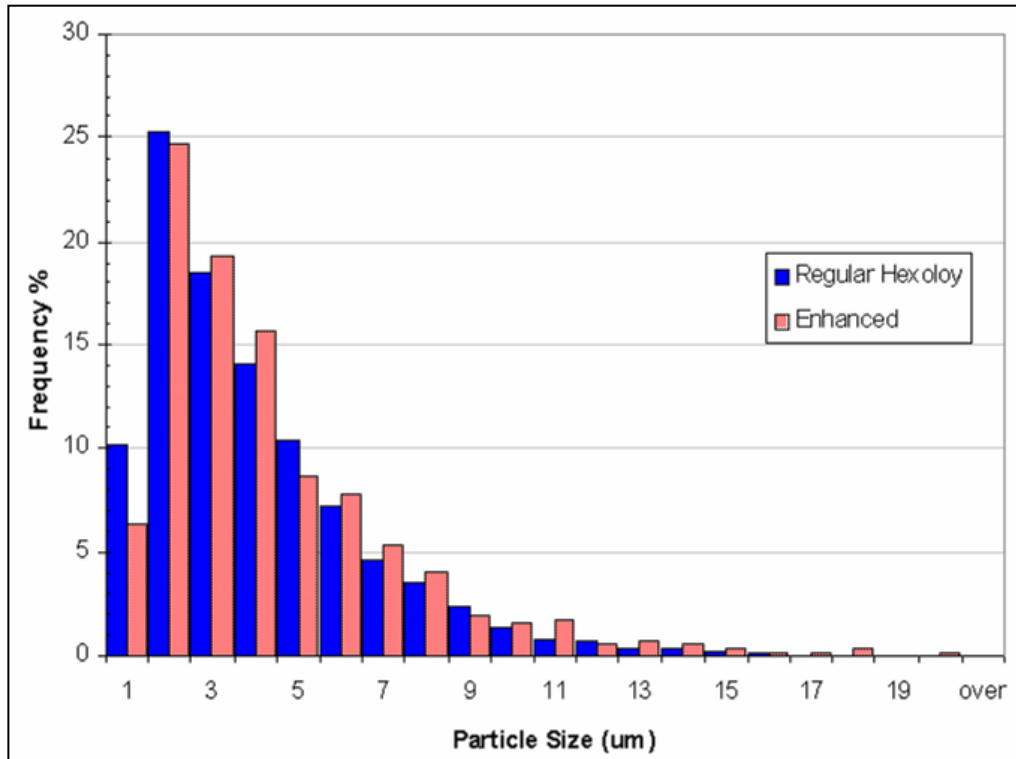


Figure 4. Grain size frequency percent distribution.

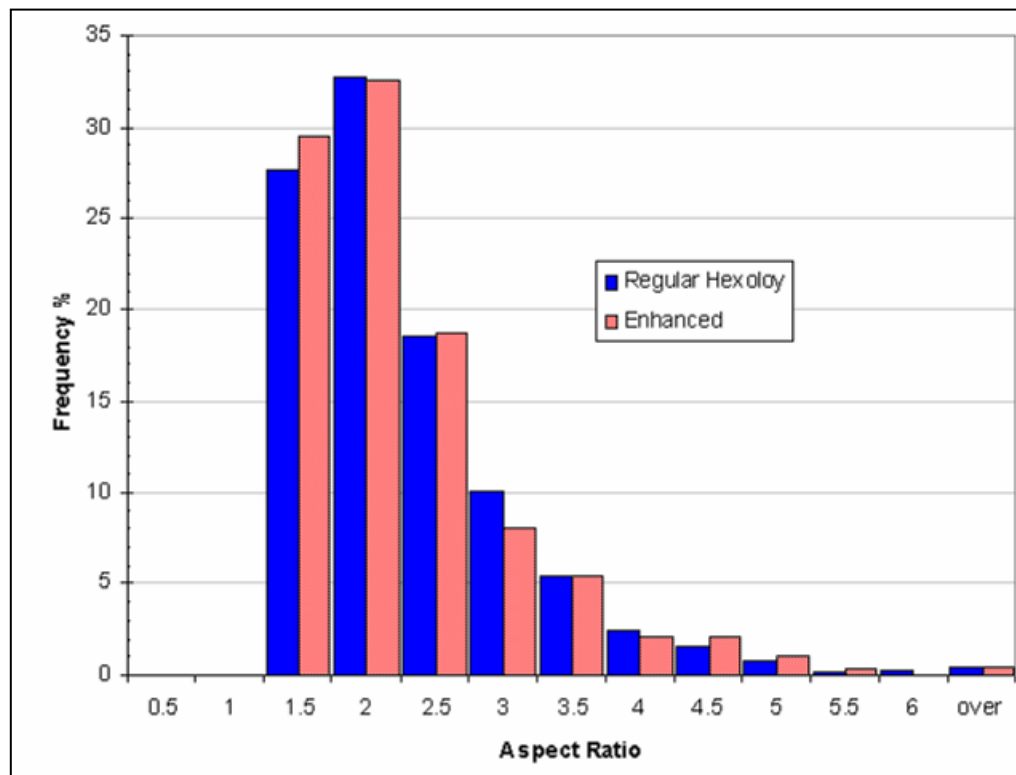


Figure 5. Aspect ratio frequency percent distribution.

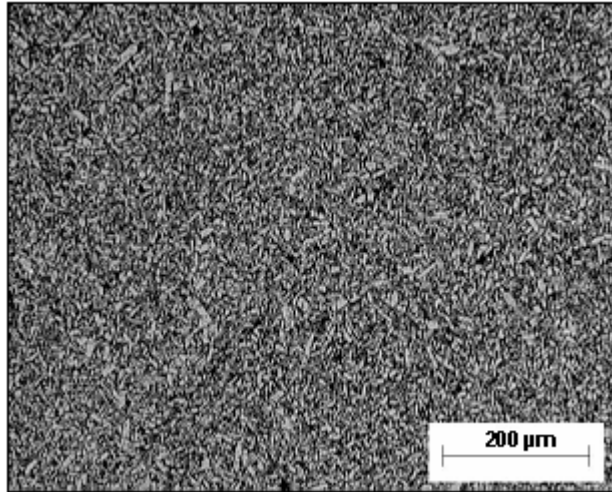


Figure 6. Regular Hexoloy 100×.

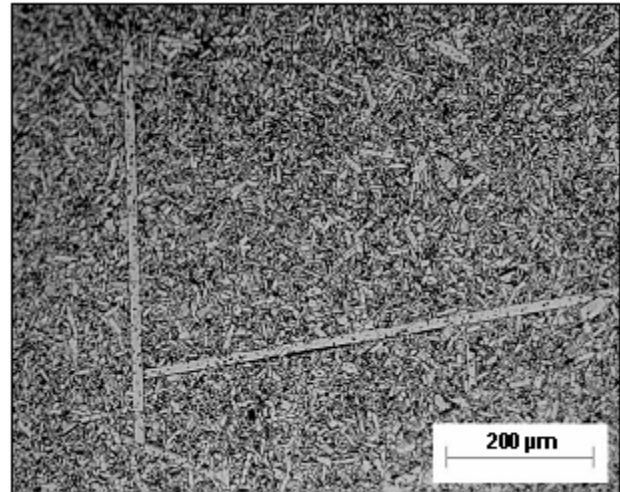


Figure 7. Enhanced Hexoloy 100×.

2.6 Determination of Pore Size Distribution and Pore Volume Percent

Un-etched micrographs were taken from polished samples of each material at 200× magnification. Figure 8 shows a micrograph of pores in RH, and EH is shown in figure 9. Since values were heavily dependent upon the quality of polish, 10 pictures were taken of the best-polished surface of each material. The same procedure used for grain sizes was used for the analysis of pores. The porosity distributions were found to differ, with RH having a higher number of large-sized pores. RH had a slightly higher total area fraction percent of pores due to its slightly lower density. This calculation took the total area of pores and divided it with the total area of micrograph. RH demonstrated 3.50%, and EH was 3.15%. Figure 10 shows pore size frequency percent distribution and figure 11 shows total pore size frequency distribution. Each figure also has a “blow-up” section on the right of the larger pore sizes since these are the critical flaws that more directly effect fracture strength. From the frequency distributions and the “blow up” section of the larger pores sizes, RH has the greater number of larger and smaller sized pores. The larger pore sizes, above 9 μm, are only seen in RH. While in proportion to the total number of pores analyzed the larger pores are small in number, the largest pores have a disproportionate and adverse effect on flexure strength. Cracks initiate from these sites and due to the brittle nature of the material, propagate and cause the material to fail. An average of the maximum pore size was also calculated from ten micrographs of each material. For EH the maximum pore size was 7.39 μm while RH was 10.10 μm. Table 2 gives a summary of the values obtained.

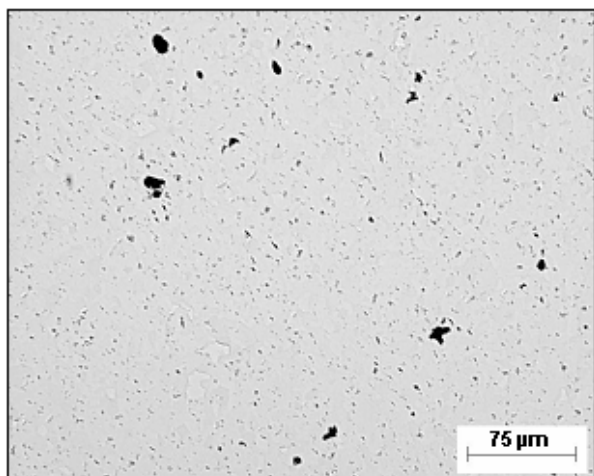


Figure 8. Regular Hexoloy 200×.

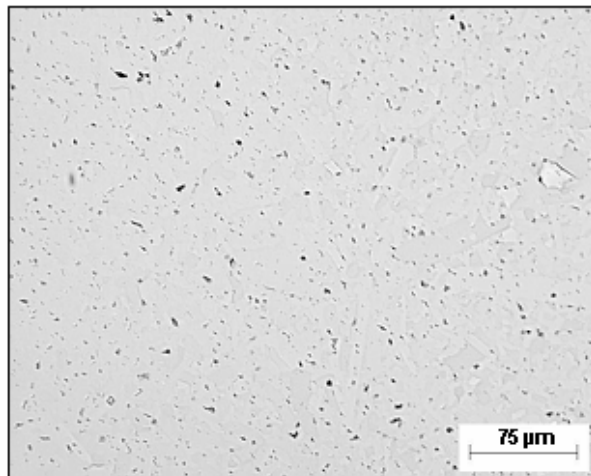


Figure 9. Enhanced Hexoloy 200×.

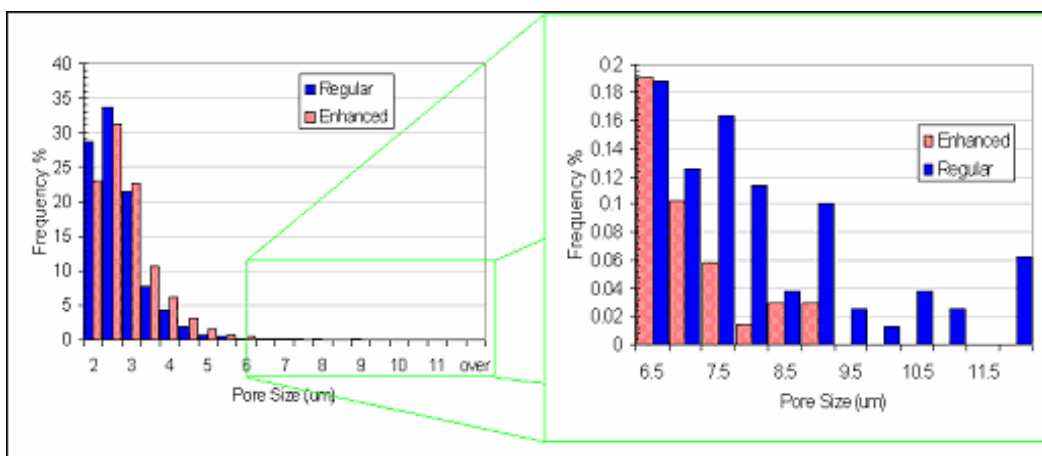


Figure 10. Pore size frequency percent distribution with blowup of larger pore sizes.

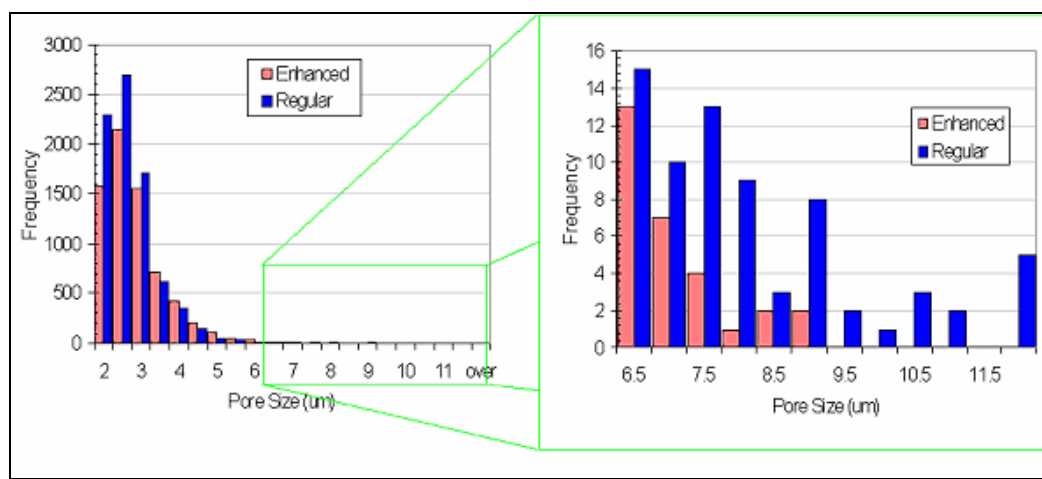


Figure 11. Pore size total frequency distribution with blowup of larger pore sizes.

Table 2. Microstructural analysis data.

	Regular	Enhanced
Avg. grain size (μm)	3.47	2.00
Avg. aspect ratio (μm)	2.05	2.00
Elongated grain area	4%	0%
Avg. pore size (μm)	2.65	2.74
Pore area frac. %	3.50%	3.19%
Avg. max pore size (μm)	10.10	7.39

2.7 Hardness

Vickers hardness testing was conducted following ASTM standard C1327 (9). Each test was run for a duration of 20 s at a 1-kg load. Five valid tests were sampled from each orthogonal face of each specimen for a total of 15 tests per material. There was no difference in the values from each orthogonal face so they were all averaged for each material. The hardness values were 23.4 ± 0.9 GPa and 23.3 ± 1.6 GPa for RH and EH, respectively.

2.8 Effect of Elongated Grains on Fracture Toughness

It was noticed that EH had a structure with elongated grains. Moberlychan et al. (10) presented a SiC with improved fracture toughness which they attributed to elongated grains. The aspect ratios of some were in excess of 10. Termed ABC-SiC, since it used Al, B, and C as sintering aids, the microstructure consisted of elongated grains formed in a complex interlocking structure with a reported fracture toughness of $9.1 \text{ MPa}\sqrt{\text{m}}$ and a four-point bend strength of 650 MPa. These two values were attained using similar methods used in this report, which will be described shortly. The grain boundaries had an amorphous phase to enhance intergranular fracture. The elongated grains enhanced crack deflection and bridging, while the interlocking structure prevented grain pullout. They noted that all the higher toughness ceramics in the literature have elongated grains.

The paper further compared the ABC-SiC to Hexoloy SA (referred to as RH in this study). From microscopy, they found fracture surfaces of four-point bend specimens to be transgranular for RH, whereas for ABC-SiC it was intergranular with crack-bridging regions behind the crack tip. Fractography of RH showed an overall smoothness similar to that of brittle glasses. Microcrack patterns from Vickers hardness indents show that the cracks in RH followed relatively straight paths, while the cracks in ABC-SiC exhibited deflections. The crack deflection and bridging caused the ABC-SiC material to have a higher fracture toughness value. The authors attributed the higher flexure strength to the higher fracture toughness.

Due to the elongated grain structure of EH, it was first believed that the material could have a higher fracture toughness value. Later tests and correspondence with the company revealed that this was not the case. The elongated grains were a by-product of sintering conditions. In fact, in Lee and Rainforth (11), they note that elongated grains could be detrimental since they provide a

larger flaw surface that lowers flexure strength. The elongated grains in EH were found to neither help nor hurt the material. Fracture strength was not adversely affected, nor was fracture toughness improved in EH.

2.9 Fracture Toughness

Fracture toughness was completed using ASTM standard C1421 (12). Single edge precracked beam (SEPB) specimens were used. Two Knoop indentations were placed across the center of the bottom face of the beams. The beams were loaded in such a manner that a sharp crack formed within a certain distance of the total height (defined as W in equation 1) of the specimen, as the standards require. The samples were then loaded to failure under the half-B configuration of ASTM standard C1161 (13) (see section 2.10). A load cell on the test frame recorded the failure load. This load, along with the average precrack length was entered into equation 1 to determine the fracture toughness.

Fracture toughness:

$$K_{Ipb} = [f(a/W)] \left[\frac{P_{\max} (S_o - S_i) 10^{-6}}{tW^{3/2}} \right] \left[\frac{3(a/W)^{1/2}}{2[1-a/W]^{3/2}} \right], \quad (1)$$

where

$$f(a/W) = 1.9887 - 1.326(a/W) - \frac{[3.49 - 0.68(a/W) + 1.35(a/W)^2](a/W)[1 - (a/W)]}{[1 + (a/W)]^2}, \quad (2)$$

where

K_{Ipb} = fracture toughness,

$f(a/W)$ = function of the ratio a/W for four-point flexure,

P_{\max} = maximum load,

S_o = outer span,

S_i = inner span,

t = thickness of specimen,

W = top to bottom dimension of specimen, and

a = pre-crack crack length.

The fracture toughness values were $2.62 \pm 0.05 \text{ MPa}\sqrt{\text{m}}$ for RH and $2.54 \pm 0.05 \text{ MPa}\sqrt{\text{m}}$ for EH. There is no noticeable difference, and the value for RH matches that of Quinn and Salem (14).

The elongated grains in EH did not have the same effect on fracture toughness as the elongated grain structure of Moberlychan et al. (10).

2.10 Flexural Strength

Flexure strength was tested according to ASTM standard C1161. Type B, four-point bend specimens with loading at quarter points were used. Roughly 20 specimens of each material were loaded to failure. This failure load was entered into the beam equation for simply supported beams and the failure stress was calculated.

Flexural strength:

$$\sigma = \frac{3PL}{4wt^2}, \quad (3)$$

where

P = break load,

L = outer support span,

w = specimen width, and

t = specimen thickness.

The specimens were found to have differing flexure strength values, with the EH being stronger. Even though Lee and Rainforth (11) stated elongated grains may decrease the strength, this was not the case in EH. EH had a flexure strength of 450 ± 40 MPa compared to RH's 380 ± 30 MPa, correlating to an 18% increase.

2.11 Discussion

The materials are very similar in all properties. See table 3 for a summary of values from the microstructural characterization. The values in parenthesis in table 3 indicate how many samples were tested. Statistically, there is little difference in density, elastic wave speeds, and fracture toughness of the materials. There is a difference in the porosity distributions and also in flexure strength values. It is believed the latter two are directly related. In the subsequent sections, it will be determined whether the differences play any part in dynamic behavior of the materials. It was interesting to note that such a small difference in pore morphology could correlate to the 18% increase in the flexure strength of EH.

There was also a small difference in area fraction percent of elongated grains. However, this was determined to have a no effect on the static properties of the materials. Either there were not enough of the elongated grains or the grain boundaries were of comparable strength to the actual grains.

Table 3. Summary of material properties.

		Regular	Enhanced
Density	(g/cm ³)	3.152 ± 0.006	3.156 ± 0.005
C Longitudinal	(km/s)	12.03 ± 0.04	12.13 ± 0.01
C Shear	(km/s)	8.21 ± 0.08	8.33 ± 0.03
C Bulk	(km/s)	8.21 ± 0.08	8.33 ± 0.03
Fracture strength (4pt-bend)	MPa	380.0 ± 30 (25)	450.00 ± 40 (22)
Fracture toughness (SEPB)	MPa√(m)	2.61 ± 0.05 (5)	2.53 ± 0.05 (5)
Vickers hardness (1 kg, 20 s)	(GPa)	23.4 ± 0.9 (9)	23.30 ± 1.6 (10)
Avg. grain size	(μm)	3.44	3.79
Pore area fract. %	—	3.50%	3.19%
Elongated grain area fract. %	—	4%	~0%
Size of largest pore	(μm)	10.10	7.39

3. Experimental Configurations

3.1 Plate-Impact Experiment

Plate-impact testing was conducted using a gas gun with a 102-mm bore diameter and 8-m-long barrel. The gun consisted of a breech, barrel, target chamber, and catch tank (figure 12). Velocities from 80 to 700 m/s were achieved, and four VISARs were available for free-surface velocity measurements. The barrel had a keyway that allowed side-by-side experiments to be conducted.

Data was collected using push-pull VISARs with the probes focused at the back surface of the specimen. Oscilloscopes collected the projectile velocity measurements and VISAR signals. A labview program interface was used for operating the gun and a separate data reduction program was used to analyze the VISAR data. The reduction program converted interference fringes to free-surface velocities.

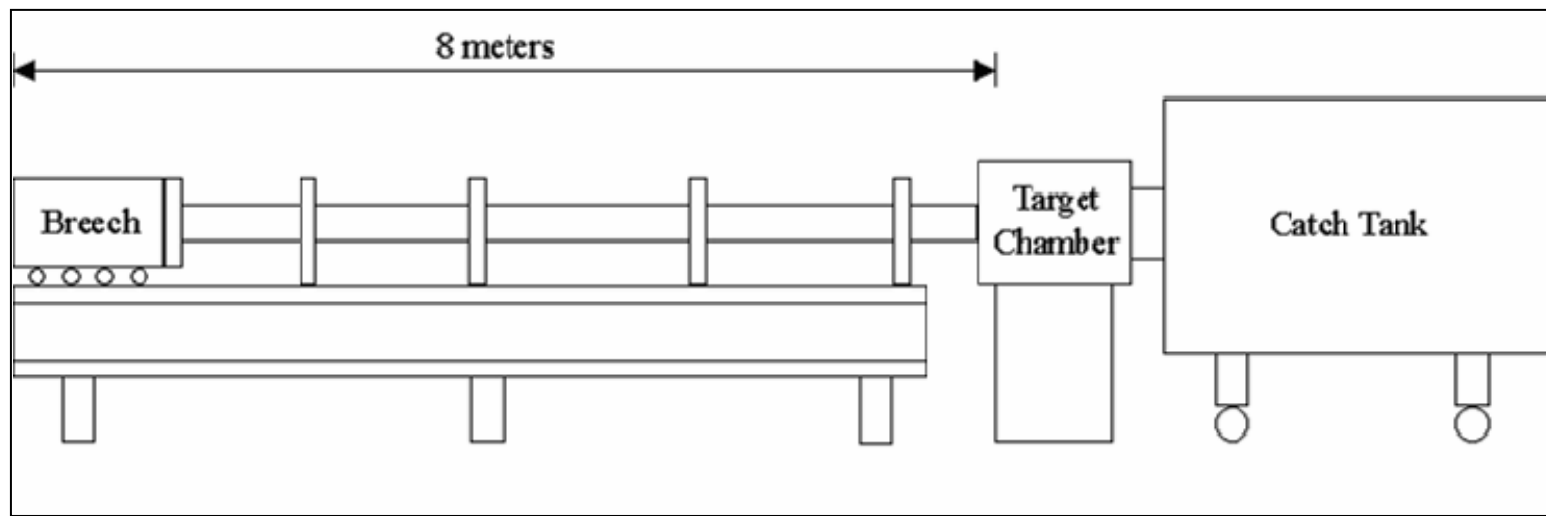


Figure 12. Gas gun schematic.

3.2 VISAR

VISAR is the acronym for Velocity Interferometer System for Any Reflector developed by Barker and Hollenbach in 1972 at Sandia National Laboratory (15). The system works off the principle of Doppler shift. A laser beam is separated into a reference and delay leg. Particle velocity at a free surface can be obtained from the interference fringes created between the two legs as a result of the movement of the reflective surface.

The system consists of a laser, a probe, a VISAR interferometer, oscilloscopes, and the necessary optic couplings and wiring. The laser beam is optically coupled to a fiber that runs into a splice box. The probe inlet is spliced to this. The probe is placed 30 mm from the reflective rear surface of the target. “Reflective” is a relative term with the optimum being between specular (mirror-like) and diffuse. The laser beam reflected from the back of the target is collected in the same probe. The beam travels back to the splice box where the output line is connected to the VISAR optical fiber (figure 13).

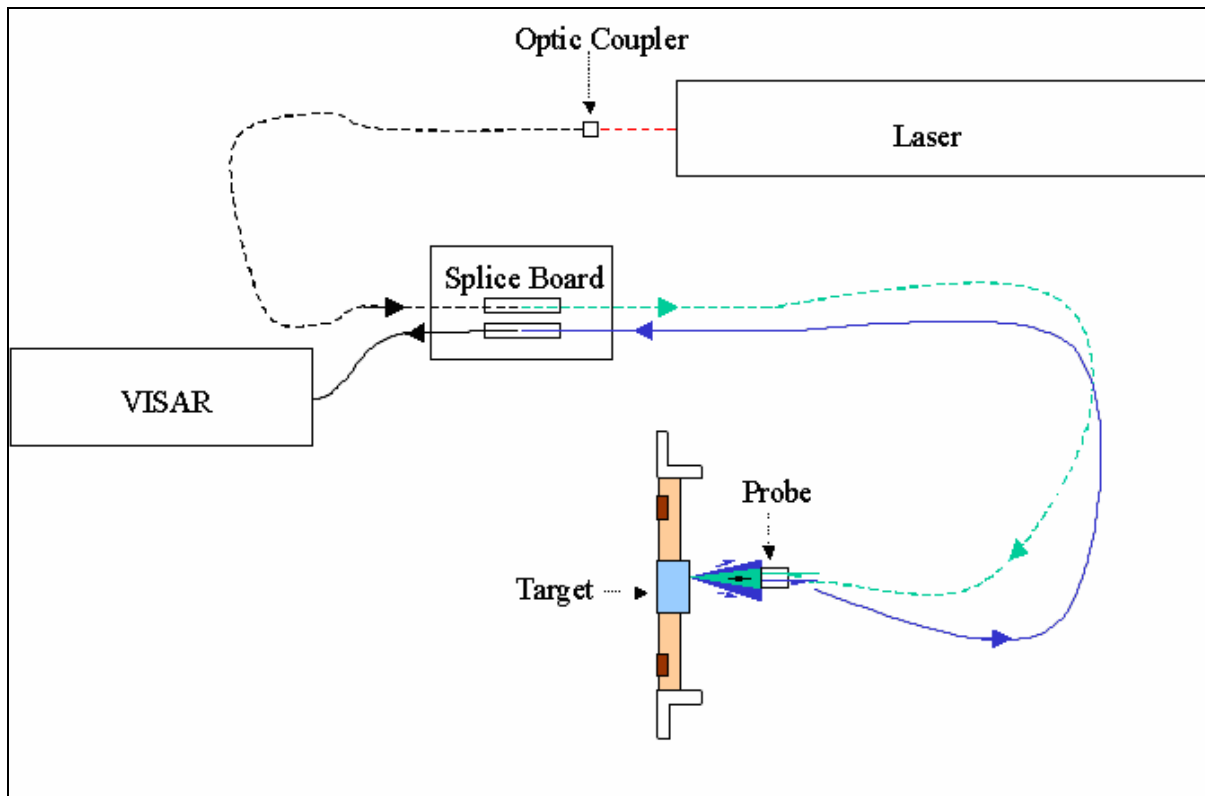


Figure 13. Probe setup.

Once in the interferometer, the beam is divided into a beam intensity monitor (BIM) and a beam that is later separated again (figure 14). The BIM is used for diagnostic purposes. The other beam is split into the reference leg and the delay leg. The delay is achieved by placing precisely calibrated glass etalons in one path of the split laser beam. The object of the delay is to achieve a

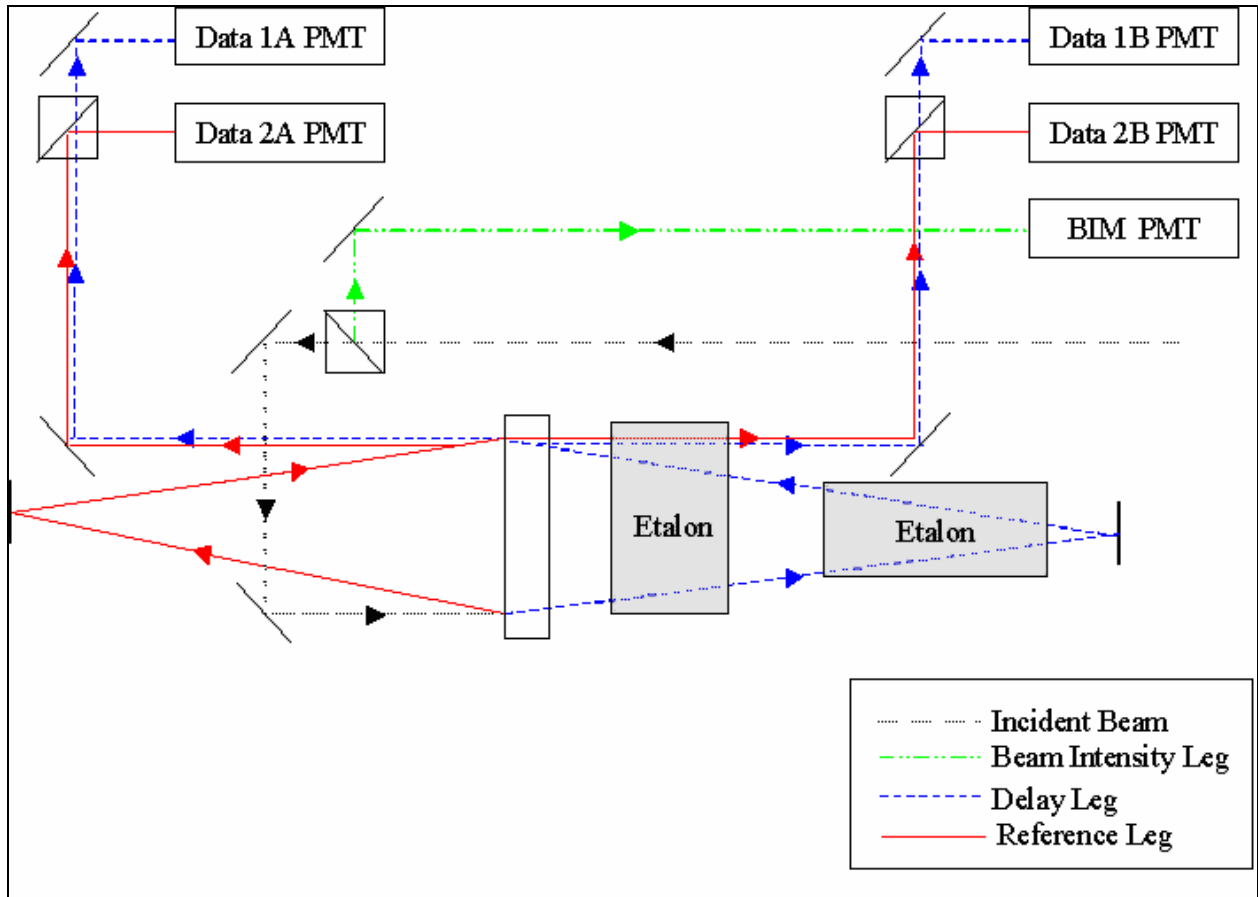


Figure 14. VISAR configuration.

90-degree phase difference between the two beams. The beams are converted into electrical signals via photo-multiplier tubes (PMT), which are connected to oscilloscopes. When the surface is moved, the reference and delay beams produce light fringes. The fringes can be correlated to free-surface velocity since the etalons have been calibrated. Final particle velocities have an accuracy of 1%.

3.3 Plate-Impact Specimens

Plate-impact specimens were machined to strict tolerances for spall tests. Cylindrical specimens were machined with thicknesses of 2.047 ± 0.003 mm, 4.047 ± 0.003 mm, and 6.397 ± 0.003 mm. Each face was flat to within three light bands, parallel to within $5 \mu\text{m}$ of the opposite face, and polished to a mirror finish. All specimens were 31.8 ± 0.03 mm in diameter.

3.4 Experimental Setup

The flyer was set in a flyer ring using epoxy. The flyer was backed with a foam plug to assure a traction-free back surface while adding stiffness. For higher velocities, an additional aluminum strap was placed on the back of the flyer ring for extra rigidity. Once the epoxy was cured, the flyer ring with flyer was epoxied onto the front end of an aluminum projectile (figure 15). The

target was assembled in a similar manner; with the target set into the target ring using epoxy. Brass contacts were also epoxied into the assembly that would serve to trigger data collection (figure 15). Figure 16 shows a front view of the flyer and figure 17 shows a front view of the target. The flyer also has a small hole drilled into the epoxy, which is not shown in figure 16, so the inner chamber of the projectile could be evacuated when a vacuum was pulled. When cured, the target assembly was attached to an adjustable mount in the target chamber at the end of the barrel. During setup, the mount was adjusted such that the target was perfectly planar to the flyer. This was accomplished using laser-alignment techniques.

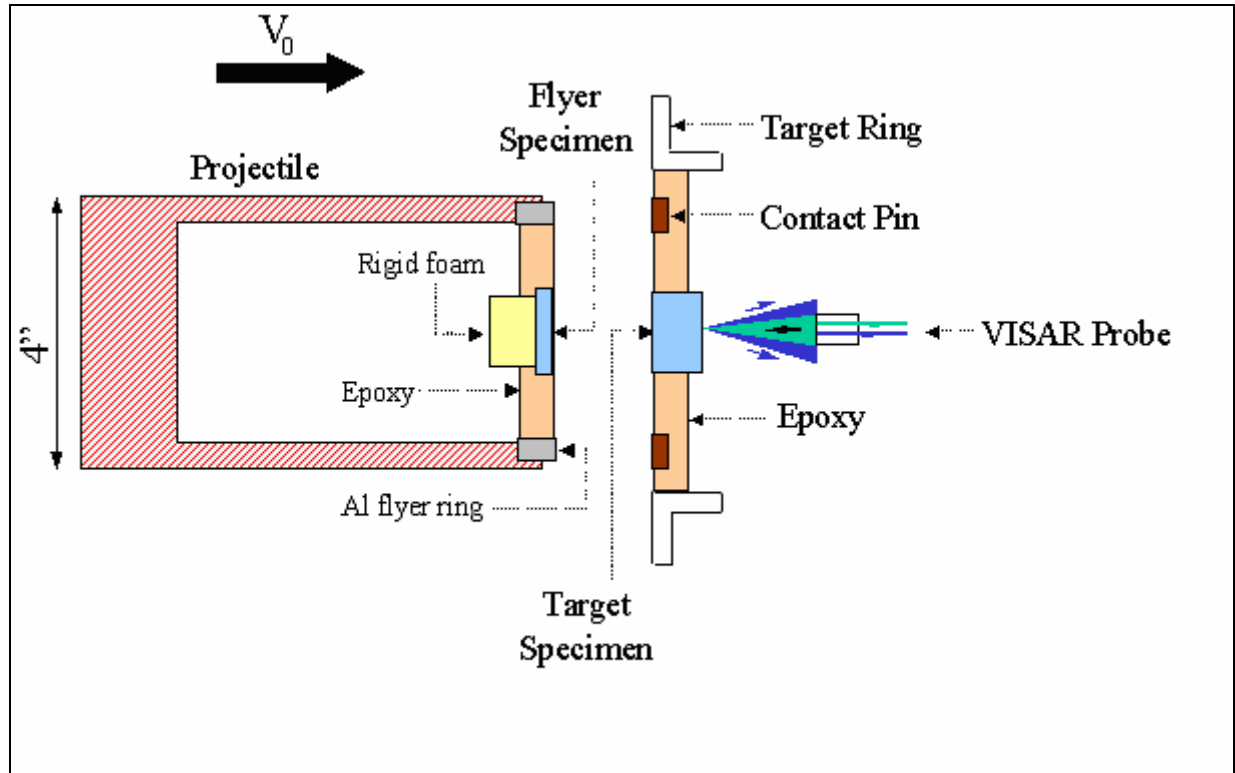


Figure 15. Diagram of cross section of projectile and target.

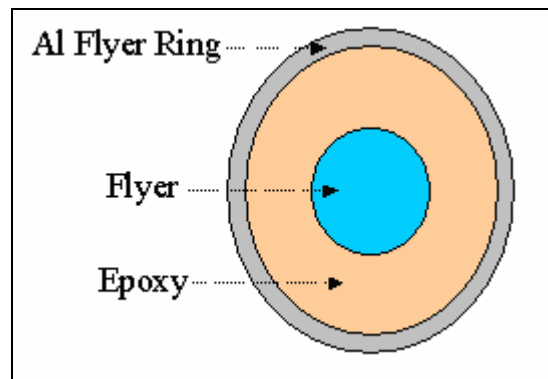


Figure 16. Front view of flyer.

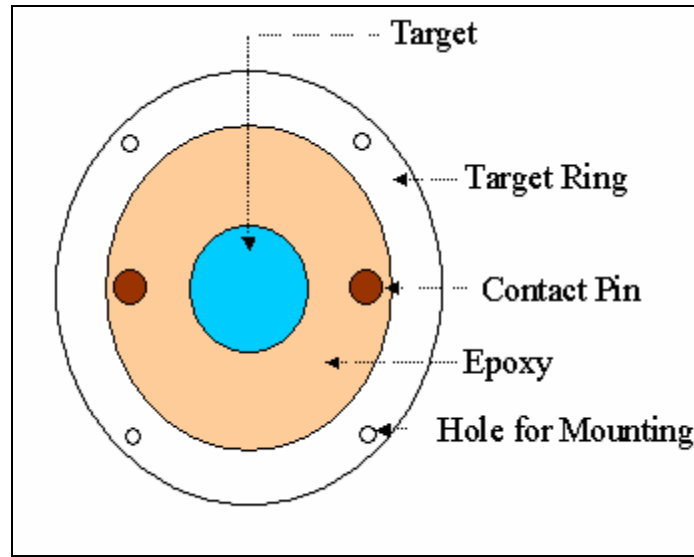


Figure 17. Front view of target.

To measure velocities, a set of four pairs of pins were arranged directly in front of the target such that when the projectile passed, the pins shorted. An oscilloscope recorded when the pins shorted, allowing velocities to be calculated. Distances between pins were accurately measured beforehand. The velocity readings from the pins were averaged to obtain the striking velocity.

For the shot, the target chamber was sealed with the probe focused on the back of the target. The catch tank was attached to the target chamber to stop the projectile and collect all the debris from the shot. A diaphragm was placed between the two chambers before each was placed under vacuum separately. The diaphragm makes the process of evacuating all the air more efficient as the two volumes of the target chamber and catch tank are much different. The chambers were then placed under vacuum to alleviate the system from the high-pressure air that would accumulate in front of the projectile otherwise.

For the shot, the projectile was placed under vacuum at the breech end of the gun. Meanwhile, the breech chamber was pressurized. When the gun was “fired,” the vacuum behind the projectile was released allowing it to be initially sucked down the tube. Once the end of the projectile passed the radial openings to the high-pressure air of the breech, the projectile attained full momentum.

3.5 Theory

For a plate-impact test, it is desirable to have one-dimensional (1-D) wave propagation to simplify analysis of material behavior. This can be achieved by making the diameter of the specimen much larger than the length. If the VISAR probe is centered on the back surface of the target, then the initial data from the experiment should be completely 1-D effects.

Assuming linear elastic properties in the material below the HEL, the 1-D waves can be tracked using the longitudinal elastic wave speed measured from ultrasonic testing. A time vs. position (x-t) plot is useful to study wave interactions and can aid in the design of experiments. Varying the thickness of the flyer controls the duration of the compressive pulse and adjusts the location of the spall plane. From the x-t diagram and initial conditions, a stress-vs.-particle velocity (σ -u) plot can be developed to determine the stress values achieved in the flyer and target throughout impact. The states in the material are found using the characteristic equations $\sigma \pm Z * u = \text{const.}$ along $dx/dt = \pm c_L$. The states of stress and particle velocity in adjacent regions are connected along straight lines of slope $\pm Z$. Thus, varying the impact velocity gives direct control of the magnitude of stress. Stress states in the materials can also be changed depending on the impedance value of the flyer. Plate-impact experiments were designed using these tools, as described in the following sections.

3.6 Spall Strength

Spall strength is defined as the amount of strength a material retains upon first experiencing tension. At impact, a shock-induced compressive wave moves through the material. Upon reaching the free surface of the target, the wave reflects as a tensile wave. Where this wave reacts with the end of the compression wave is where the target first experiences tension. If the stress is above the spall threshold, cracks will initiate and coalesce along a spall plane. The spall plane creates a free surface and causes additional reflections. Wave reflections can be observed by the VISAR at the free surface of the target.

Spall strength can vary with impact stress and duration of compressive pulse. The former is believed to be a result of the magnitude of compressive damage; the latter provides information on the time-dependent damage experienced by the material throughout the initial compressive wave.

When impacted, if the stress does not exceed the spall threshold value, then the free-surface velocity will return to zero, indicating there was no spallation. If the stress is high enough to induce spallation, then a drop in velocity will occur. Shortly thereafter, the velocity will rise again indicating the stress wave has reflected off the newly created surface within the target. The magnitude of this drop from the initial Hugoniot stress state indicates the spall strength. If the velocity profile never decreases, there is no spall strength in the material.

3.7 Identification of Spallation on an X-T Diagram

The x-axis of an x-t diagram indicates position, with zero defined as the interface between the flyer and target. The y-axis indicates time, with zero defined as the moment the flyer impacts the target. Upon impact, compression waves propagate into both the flyer and target at their respective longitudinal elastic wavespeeds. This is represented on the x-t diagram by drawing lines with slope $1/c_L$ back into the flyer and into the target (figures 18 and 19). Figure 18 is the x-t diagram of EH with a 2-mm flyer and figure 19 is EH with a 4-mm flyer. All lines within the

flyer should be of slope $1/c_L$ of the flyer, and all lines within the target should be of slope $1/c_L$ of the target. The compressive waves reflect off the free surfaces and travel back into the materials as tensile waves. The tensile wave in the target is called a release wave. For a symmetric impact, where both the flyer and target are the same material, the tensile wave from the flyer represents the end of the compressive pulse. The time (y-value) where this wave hits $x = 0$ is considered the pulse width, denoted pw in figures 18 and 19. Pulse width can also be calculated using equation 4. The line representing the end of the compressive pulse is extended into the target. Where this line intersects the release wave within the target indicates the position and time the material will first experience tension. Spallation will occur at this time and location. For a symmetric impact, spallation within the target will occur exactly one flyer thickness from the free surface.

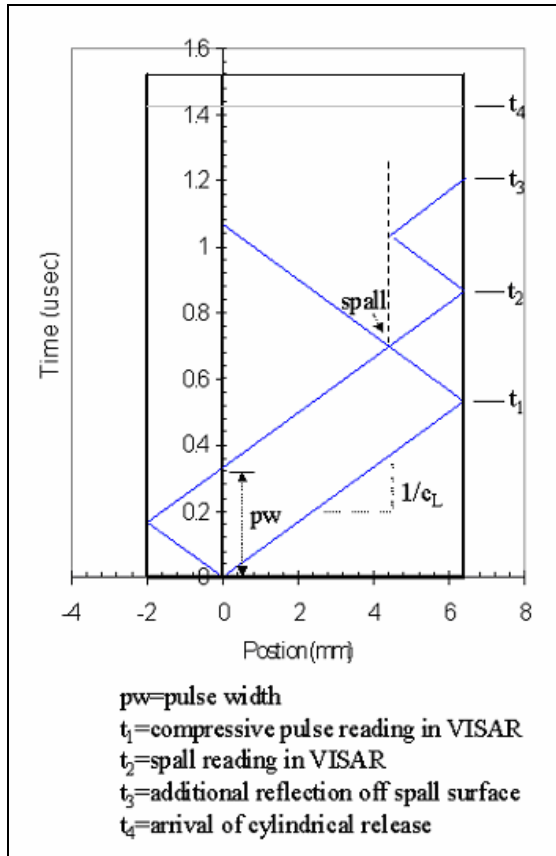


Figure 18. X-T diagram 2-mm flyer.

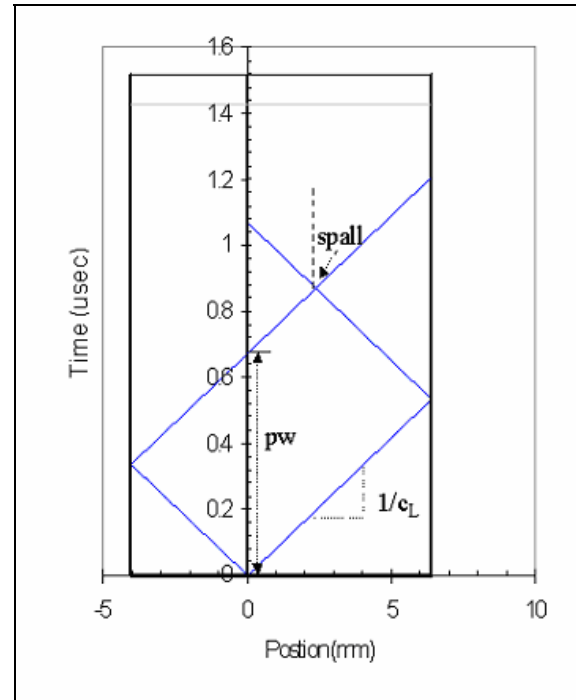


Figure 19. X-T diagram 4-mm flyer.

Pulse width:

$$pw = 2 * \frac{th_{flyer}}{c_{L_flyer}}, \quad (4)$$

where

pw = pulse width,

th_{flyer} = thickness of flyer, and

c_{L_flyer} = longitudinal wave speed of flyer.

3.8 Estimate of Spall Strength From Free-Surface Velocity Profile

A graphical method was employed to calculate spall strength. Knowing the impedance of the flyer and target and also knowing the impact velocity, a σ -u graph (figure 20) was formulated. The target material starts at velocity 0 and the flyer begins at the striking velocity. Both materials experience no stress before impact. Upon impact, the stress state achieved is the intersection of the lines formed by the impedances. The state in the material at this point is termed the Hugoniot state. The target starts at (0,0) and moves to the right with a slope of its impedance. The flyer moves from ($V_{striking}, 0$) backwards at a slope of minus its impedance. The y-value of this intersection indicates the impact stress. The x-value of the intersection is the particle velocity at impact. For symmetric impact, this value is half of the impact velocity. The target moves to the right from this intersection at a slope of minus its impedance. The target will unload and the stress will be zero, however, the particle velocity will not be zero. The particle velocity can be measured at the free surface of the target using the VISAR. For a symmetric impact, the free-surface velocity should be the same as the Hugoniot velocity measured by the VISAR. The change in velocity from the Hugoniot state to the dip in the VISAR free-surface velocity profile is used to calculate the spall stress. This change in velocity is called pullback, as shown in figure 21. On the σ -u diagram, pullback is subtracted from the particle velocity of the target and two lines of slope of \pm the target impedance are drawn underneath in the minus y region, indicating tension. The y-value of this intersection is the spall strength of the material at that impact velocity. Spall strength can also be calculated using equation 5.

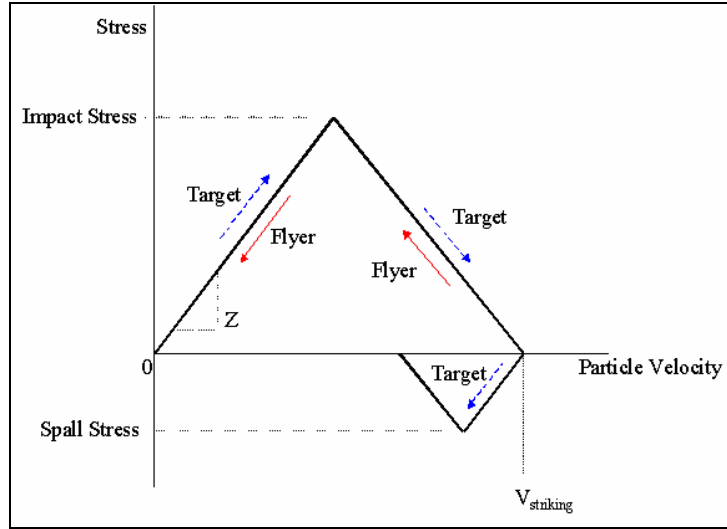


Figure 20. Stress vs. particle velocity diagram.

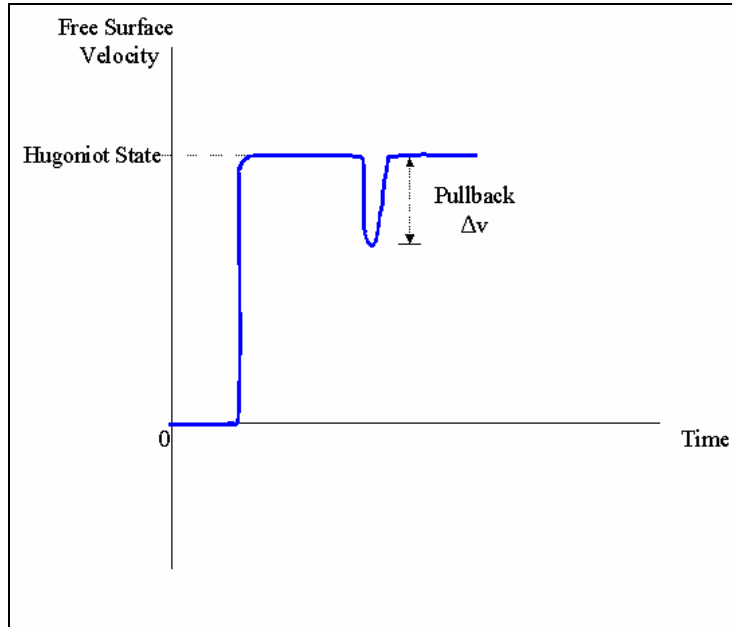


Figure 21. Free-surface velocity vs. time diagram.

Spall:

$$\sigma_{spall} = \frac{1}{2} \Delta v * Z_{tar} , \quad (5)$$

where

Δv = pullback and

Z_{tar} = elastic impedance of target.

3.9 Experimental Configuration for Determining Spall Strength

All spall tests at impact stresses below the HEL were symmetric, with flyer and target of the same material. Tests were completed with flyers of nominal thickness: 2 and 4 mm. This was done to achieve two different pulse widths to test for time-dependence of damage within the samples. Targets were 6.4 mm thick. Figures 18 and 19 show how pulse width changes with flyer thickness. All SiC samples were 31.8 mm in diameter. This l/d ratio was such that cylindrical release waves would not interfere with the measurement of the longitudinal waves. The time before arrival of the cylindrical wave is calculated as follows:

$$t_{cylindrical} = \frac{\sqrt{th_{tar}^2 + (d_{min}/2)^2}}{c_{L_tar}}, \quad (6)$$

where

$t_{cylindrical}$ = time when cylindrical wave arrives,

th_{tar} = thickness of target,

d_{min} = the lower of the diameters between the flyer and target, and

c_{L_tar} = longitudinal wave speed of the target.

The diameters were also such that two samples could be fired side by side in one shot. For side-by-side shots, two probes and two VISARs were used, one for each sample. Testing this way had the increased benefit of allowing two tests to be run at exactly the same conditions (i.e., identical striking velocity).

Specimens were placed side by side on most shots. For one shot, EH and RH, each with identical flyer thicknesses, were tested simultaneously. The majority of the other side-by-side shots were conducted using the same material but with different pulse widths. Side-by-side testing required a key to be placed on the projectile to prevent spinning of the projectile during the shot. A key was used for single shots as well.

3.10 Experimental Configuration for Determining Spall Strength Above HEL

Due to the limitations of the gas gun, in order to achieve an impact stress above the HEL it was necessary to switch the flyer to a higher-impedance material. A symmetric impact would require a velocity beyond the pressure ranges of the gun. The higher-impedance material forces the impact stress to increase (figure 22). The calculation for impact stress above the HEL is slightly different from the previously described process.

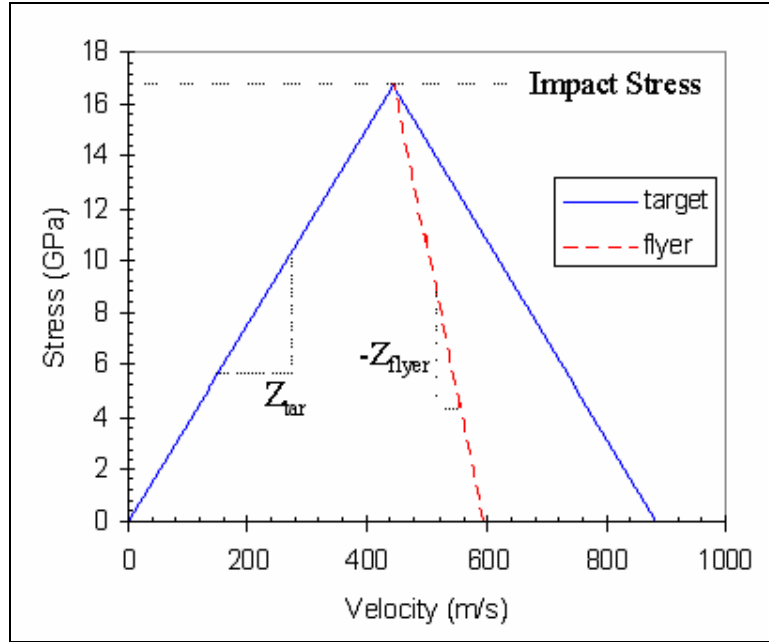


Figure 22. Stress vs. velocity with impedance mismatch (purely elastic response).

The impedance of the material changes upon reaching the HEL to the plastic impedance, which is merely the bulk sound speed multiplied by the density. This can be represented graphically on a σ - u diagram by having the target go from (0,0) at a slope of Z_{el} to the HEL. At this point, the slope becomes Z_{pl} . In all likelihood, the HEL of the projectile will be exceeded as well. The same technique is employed with Z_{el} and Z_{pl} of the flyer. The intersection of the plastic impedances of the target and flyer give an estimate of the impact stress achieved. The target will unload elastically and the slope is simply $-Z_{el}$. Figure 23 gives an example of such an analysis.

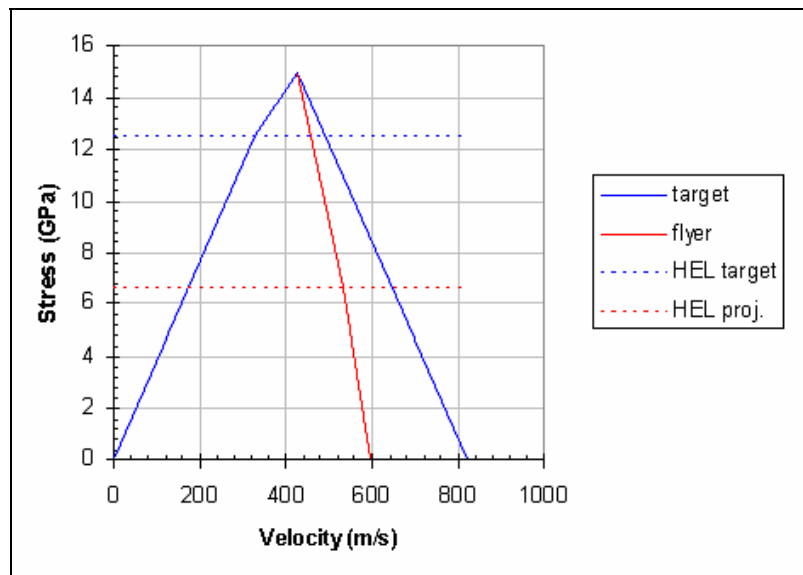


Figure 23. Stress vs. velocity using material elastic-plastic response.

K68, a tungsten alloy with cobalt binder produced by Kennametal, was used as the higher-impedance material in shots 0405H and 0408H. For K68, the previous assumption for calculating impact stress was invalid. Instead, the Hugoniot curve was known, and instead of the Z_{el} and Z_{pl} slopes, the actual curve was placed in the stress-vs.-particle velocity graph. The intersection of the Hugoniot curve and Z_{pl} of the target gave a reasonable prediction of the impact stress. Figure 23 shows an analysis of shot 0405H. A simple check is to compare the predicted target particle velocity in the released state from the σ -u diagram with the measured Hugoniot state free-surface velocity measured from the VISAR.

3.11 HEL

According to Grady (16), the HEL “identifies the axial stress at which a solid, loaded-in compression under constraint of uniaxial strain can no longer support elastic distortion and begins to flow through plastic or cataclastic (crushing) fracture processes.” Bourne et al. states, “most authors agree that the HEL for a ceramic provides a threshold below which the material retains some cohesion and has finite spall strength and above which the material has zero spall strength and becomes an inertially confined powder” (17).

HEL can be seen on free-surface velocity graphs and is represented by a slope change on the rise to the Hugoniot state. The free-surface velocity at the break in elastic rise is used to calculate the HEL. Equation 7 calculates HEL:

$$HEL = \frac{v^* Z_{el}}{2}. \quad (7)$$

Originally, HEL experiments were attempted with 6.4-mm-thick targets. However, the transition from elastic to plastic was not very pronounced. Therefore, thicker target specimens were prepared to exaggerate this effect and make the transition more visible. Tungsten carbide (WC) from Cercom was used with 9.9-mm-thick SiC targets. The elastic-plastic responses of WC and SiC were adequate to calculate impact stress (figure 24).

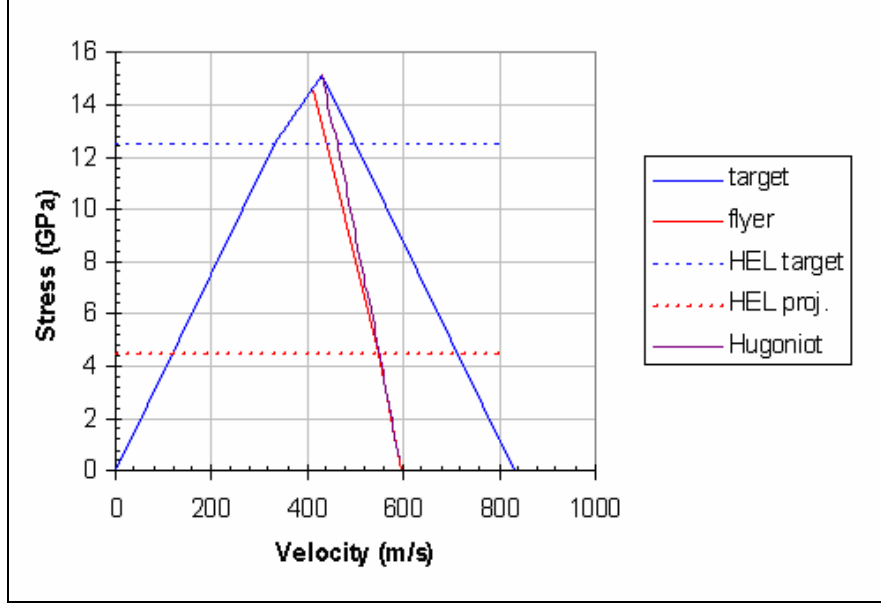


Figure 24. Stress vs. velocity using elastic-plastic response of target and Hugoniot curve of flyer.

4. Results

4.1 Spall Strength

Spall tests were conducted at four different velocities: 200, 300, 400, and 600 m/s. Impact stresses were calculated to be ~4, 6, 8, and 15 GPa, respectively. Experiments for the first three impact velocities were conducted at two different pulse widths. Table 4 shows a shot summary. The pulse widths were calculated using equation 4. For the 2-mm flyers, the pulse width was ~340 ns; for the 4-mm flyers, it was ~670 ns. The tests at 600 m/s were conducted using K68. The thickness of each K68 flyer created pulse widths within 36 ns of the 2-mm SiC pulse width. Table 5 shows pulse-width values. The density of K68 was 14.92 g/cm^3 , with c_L being 6.92 km/s, c_S being 4.16 km/s, and c_o calculated as 4.98 km/s (unpublished data).

Table 4. Shot summary.

Shot No.	Flyer t (mm)	Targ. T (mm)	Impact Vel. (km/s)	Impact Stress (GPa)	Pullback (m/s)	Spall (GPa)	HEL (GPa)
Enhanced Material							
323G	2.048	6.392	302.9	5.80	43.3	0.830	—
328G	2.050	6.401	407.8	7.81	34.1	0.653	—
411H	2.050	4.045	200.8	3.84	43.7	0.836	—
321H	4.044	6.398	302.9	5.80	42.2	0.807	—
324G	4.048	6.400	199.8	3.82	26.8	0.513	—
408H ^a	1.289	6.398	601.9	15.30	14.4	0.276	13.9
412H ^b	3.999	9.854	607.0	15.30	—	—	13.1
Regular Material							
323H	2.045	6.397	302.9	5.74	34.6	0.657	—
325G	2.051	6.396	203.4	3.86	32.5	0.615	—
327H	2.043	6.393	203.4	3.86	32.5	0.615	—
403G	2.050	6.402	302.6	5.74	37.6	0.712	—
403H	2.048	6.397	302.6	5.74	35.3	0.669	—
322H	4.049	6.401	302.3	5.73	37.4	0.709	—
325H	4.052	6.397	203.4	3.86	28.6	0.542	—
327G	4.049	6.398	406.7	7.71	32.5	0.616	—
405H ^a	1.288	6.396	593.7	15.10	15.2	0.288	13.6
410H ^b	4.002	9.929	598.6	15.10	—	—	13.9

^aFlyer was K68.^bFlyer was WC.

Table 5. Pulse widths and times to arrival of cylindrical wave.

Shot No.	Flyer t (mm)	Targ. T (mm)	Pulse Width (μ s)	Arrival Cyl. Wave ^a (μ s)
Enhanced Material				
323G	2.048	6.392	0.338	1.421
328G	2.050	6.401	0.338	1.421
411H	2.050	4.045	0.338	1.361
321H	4.044	6.398	0.667	1.421
324G	4.048	6.400	0.667	1.421
328H	4.045	6.393	0.667	1.421
408H ^b	1.289	6.398	0.373	1.421
412H ^c	3.999	9.854	1.134	1.549
Regular Material				
323H	2.045	6.397	0.340	1.413
325G	2.051	6.396	0.341	1.413
327H	2.043	6.393	0.340	1.413
403G	2.050	6.402	0.341	1.413
403H	2.048	6.397	0.340	1.413
322H	4.049	6.401	0.673	1.413
325H	4.052	6.397	0.674	1.413
327G	4.049	6.398	0.673	1.413
405H ^b	1.288	6.396	0.372	1.413
410H ^c	4.002	9.929	1.135	1.548

^a t_d from figure 18.^bFlyer was K68.^c Flyer was WC.

Spall strengths were plotted as a function of impact stress in figure 25. The square symbols represent experiments conducted with 2-mm-thick flyers, while the circles were conducted with 4-mm flyers. The solid symbols represent EH while the hollow symbols represent RH. The triangular symbols represent the spall tests conducted using K68 flyers. The asterisks in the legend are simply to point out that the K68 flyers had pulse widths equivalent to 2 mm of SiC.

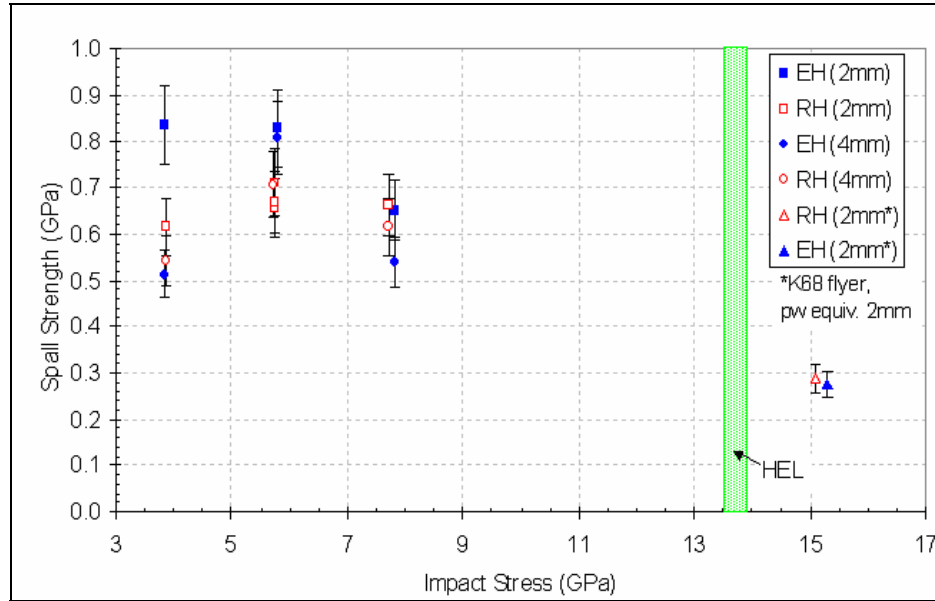


Figure 25. Spall strength vs. impact stress.

Shots 323G, 328G, and 411H were conducted on EH at 302.9-, 407.8-, and 200.8-m/s striking velocities, respectively (figure 26). Table 4 shows corresponding impact-stress calculations. The flyers were all EH with a thickness of 2 mm. Shot 411H was conducted with a 4-mm target. Shot 411H had an abnormally large spall strength, which will be discussed later. Shot 408H was conducted to determine both HEL and spall strength. The striking velocity of 601.9 m/s was chosen to result in an impact stress above 15 GPa, well above normal values for HEL in SiC (usually 12–14 GPa). The HEL will be discussed in section 4.2. Shots 321H, 324G, and 328H were symmetric impacts, each using an EH flyer thickness of 4 mm, as the results show in figure 27. The striking velocities for those shots were 302.9, 199.8, and 407.8 m/s, respectively. Figure 28 shows the effect of pulse width on the free-surface velocity profiles. Spallation occurs sooner with the 2-mm sample (shot 323G) and, in figure 28, a wave reverberation from the newly created spall plane is apparent. The “H” and “G” in the shot designations simply refer to the VISAR used in the experiment. If two shots were conducted side by side as previously discussed, the shot number will be the same, however, one specimen will have used the “H” VISAR and the other will have used the “G” VISAR.

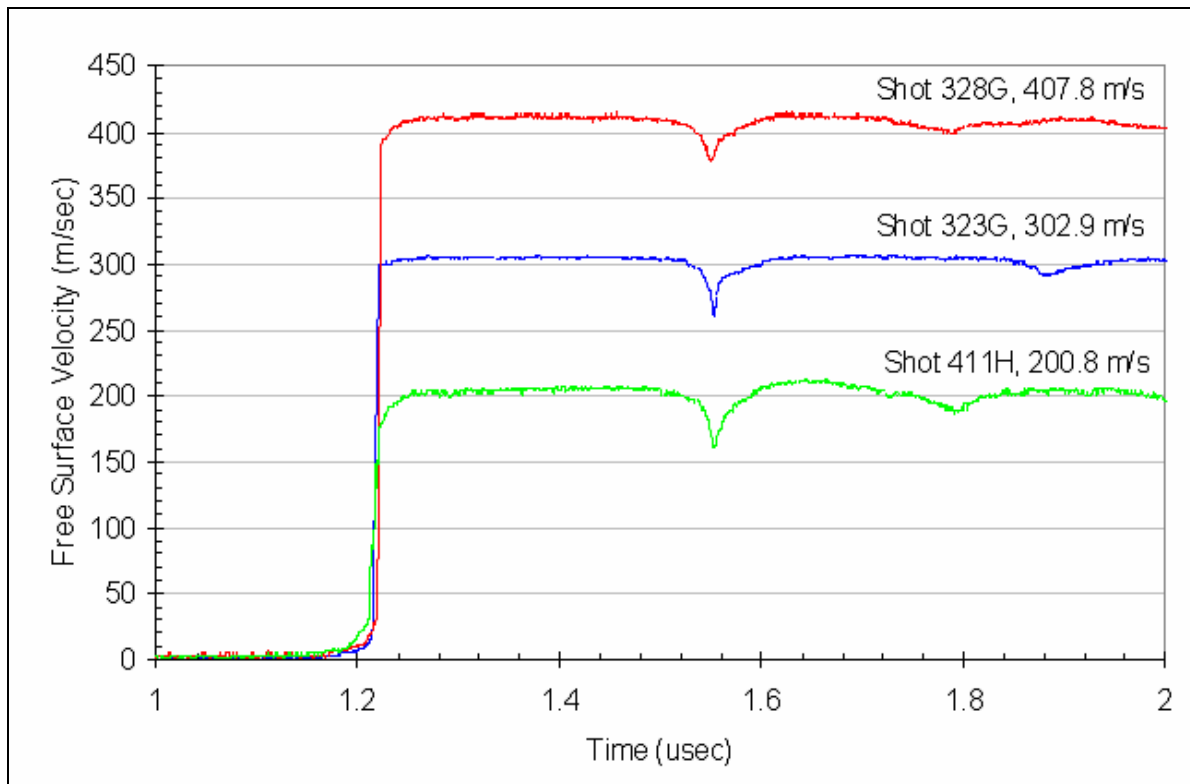


Figure 26. Free-surface velocity profiles of EH with 2-mm flyers.

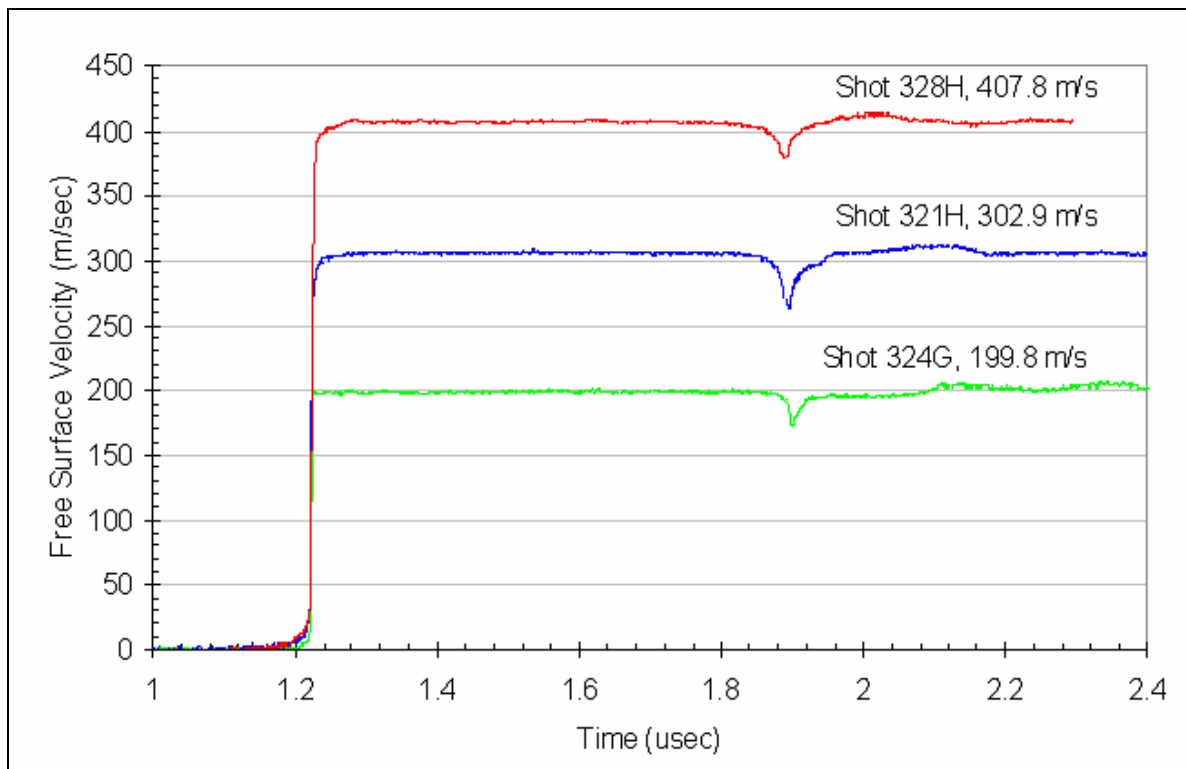


Figure 27. Free-surface velocity profiles of EH with 4-mm flyers.

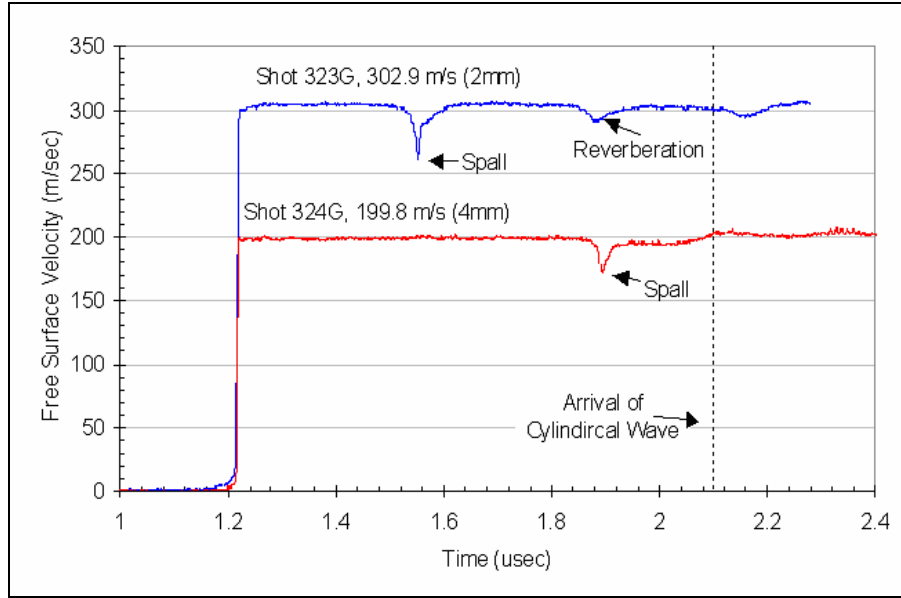


Figure 28. Free-surface velocity profiles of EH with 2- and 4-mm flyers.

For RH, shots 323H, 325G, 327H, 403G, and 403H were symmetric impacts with 2-mm-thick flyers (figure 29). The impact velocities were 302.9, 203.4, 406.7, 302.6, and 302.6 m/s, respectively. Shots 403G and 403H replicated the conditions of shot 323H to test for repeatability in the spall-strength measurements (figure 30). The results fell within the error bars of the original (figure 25). Shots 322H, 325H, and 327G were RH shots conducted with 4-mm flyers at 302.3-, 203.4-, and 406.7-m/s striking velocities, respectively (figure 31). Shot 405H was conducted with K68 as the flyer at a striking velocity of 593.7 m/s. Shot 405H was conducted to obtain both spall and HEL.

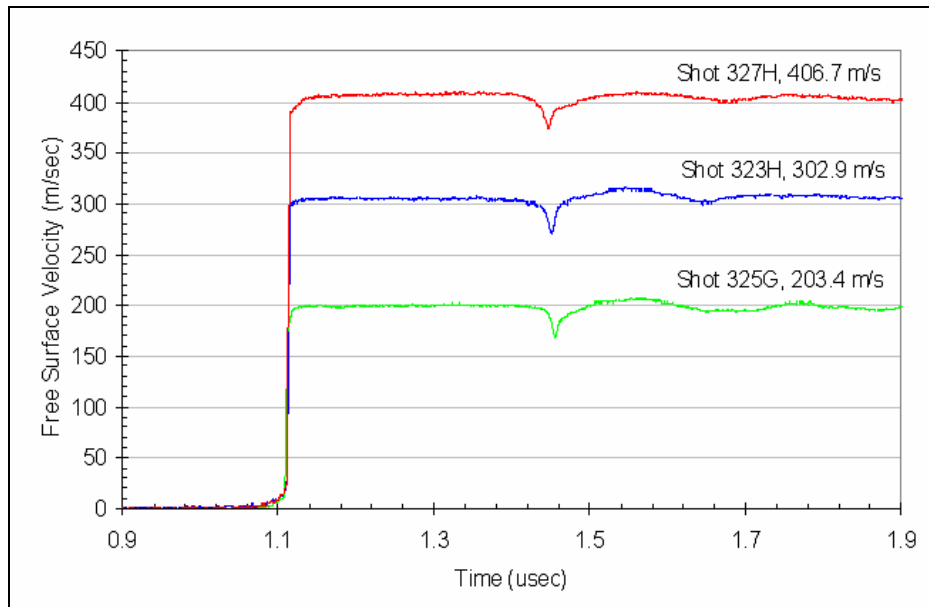


Figure 29. Free-surface velocity profiles of RH with 2-mm flyers.

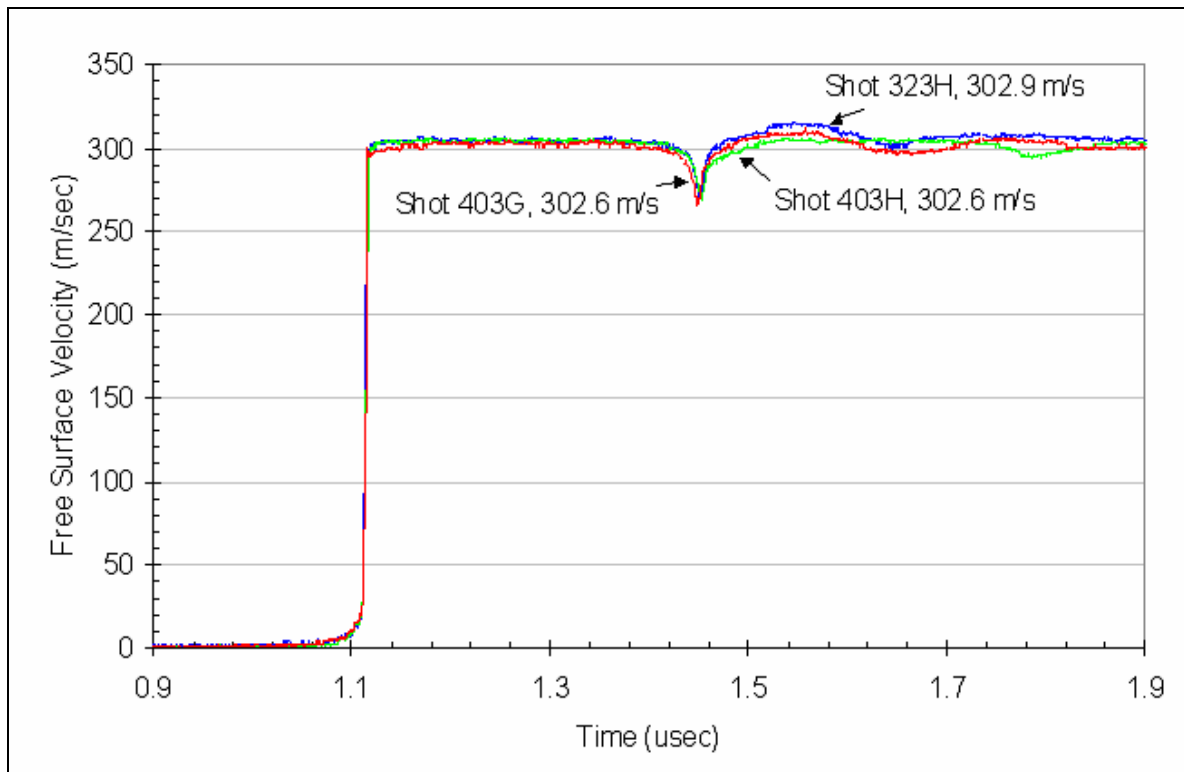


Figure 30. Repeatability tests, RH at ~300m/s with 2-mm flyers.

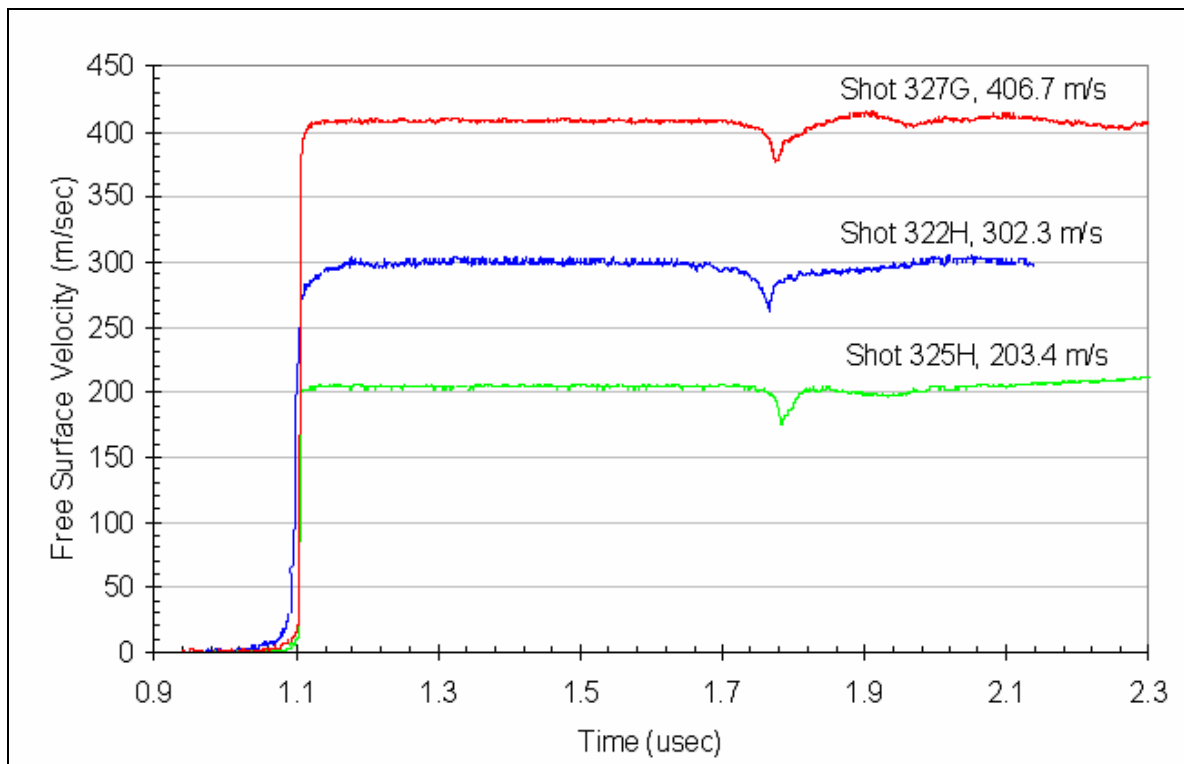


Figure 31. Free-surface velocity profiles of RH with 4-mm flyers.

Shot 0411H seems to be an anomaly in that all the other shots follow a similar trend, with little pulse-width dependence, and little difference between the materials. The EH target in shot 0411H has a much higher spall strength than the similar test with the longer pulse width (324G) and than those of RH (325G and 325H). The only reasonable explanation is that the result is one of material variability. Dandekar had similar results in his study (18, 19).

Spall-strength results show similar trends to those found in Dandekar (18, 20). Spall strengths increase up to a threshold in impact stress and then show a subsequent decline (figure 25). Dandekar initially attributed this to competing damage mechanisms. Below the threshold, plasticity dominated; above it, crack dynamics determined spall strength (20). Recently, Dandekar performed simultaneous compression-shear plate-impact experiments which supported the assumption that plasticity dominates deformation below the threshold (19). However, he found that, above the threshold, deformation mechanisms become much more complex with the presence of a failure wave under induced shear. The threshold impact stress for RH and EH appears to be around 5.8 GPa. At impact stresses above the HEL, the materials retain finite spall strengths. The post-HEL spall strength is lower than the other values.

For the most part, the longer pulse-width experiments show slightly lower spall strengths. However, within the variability of the tests, spall strength could be considered pulse-width independent. The exception could be EH at an impact stress of 8 GPa. It would be interesting to explore that the material might not become pulse-width dependent until a certain threshold stress has been achieved. One possible explanation could be that the failure mechanism before the threshold impact stress is time-independent, but, above it, another failure mechanism is time-dependent. The experiments on RH at 5.8 GPa obtained spall-strength results where the longer pulse width had a higher spall strength. However, those results are within the variability of the tests.

Experimental error was calculated using error propagation routines discussed by Taylor (21). The error associated with the VISAR measurement was used in conjunction with the errors associated with the density and longitudinal elastic wave speed measurements to determine the error bars associated with the calculated spall-strength values.

4.2 HEL

As previously discussed, shots 405H and 408H were designed to determine both spall strength and HEL. The two shots were conducted with a striking velocity near 600 m/s. There was not a clear transition from elastic to plastic rise in the free-surface velocity profile. Thicker specimens were used in shots 410H and 412H in an attempt to exaggerate the transition. WC samples from Cercom were used for flyers in these experiments. The WC flyers were thicker, so the experiments were conducted strictly for the purpose of determining HEL. Material data for the Cercom WC can be found in Dandekar and Grady (22). Shot 410H was conducted on RH at a striking velocity of 598.6 m/s and shot 412H on EH at 607.8 m/s. Unfortunately, the elastic-plastic transition in the latter two tests had results similar to the tests conducted with K68.

Figure 32 shows HEL results on RH, and figure 33 shows HEL results for EH. Despite not having a clear transition, HEL values could be determined from the profiles since there was a rapidly increasing linear portion to the rise, followed by a slower sloping continuation to the Hugoniot. The HEL was taken to be this transition point. The free-surface velocity profiles were similar to those obtained by Feng et al. (23) without a distinctive transition from elastic to plastic at the HEL. A possible explanation is that the plastic wave only began to form at the impact velocities tested. Higher impact stresses would allow the transition to develop. Plots with a significant transition from elastic to plastic wave rise similar to Grady's (24) require much higher impact velocities which are not achievable with the current test facilities at ARL.

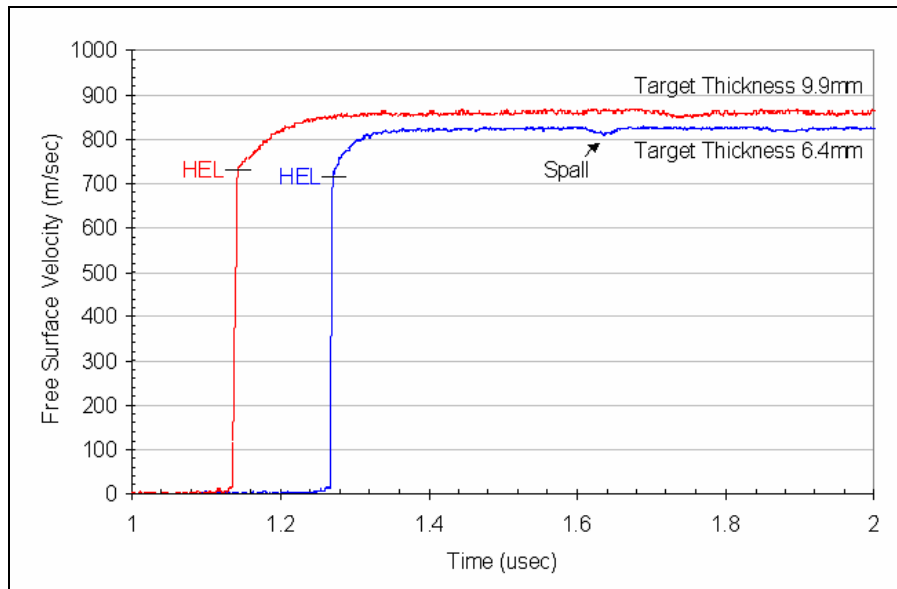


Figure 32. HEL profiles for RH.

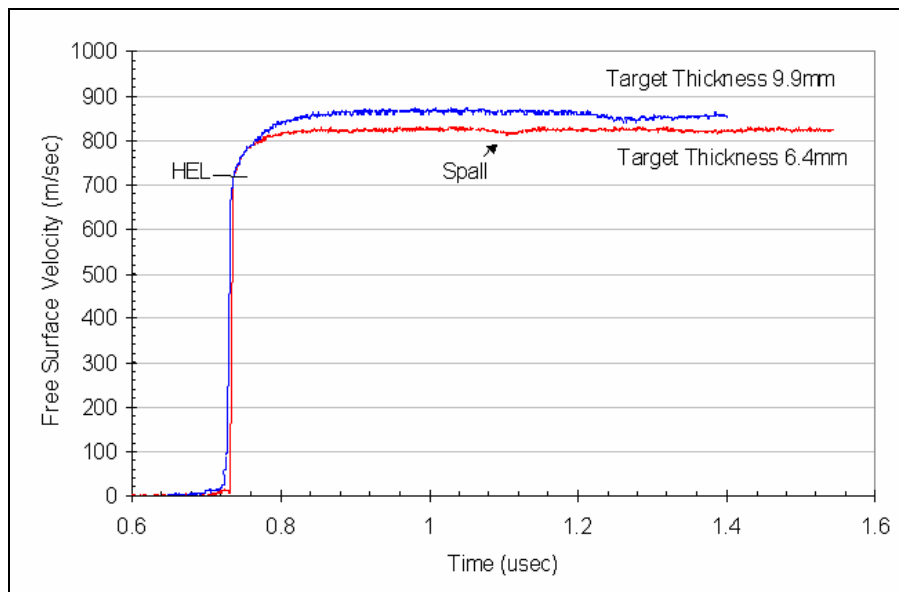


Figure 33. HEL profiles for EH.

At impact stresses of 15.1 and 15.3 GPa, RH and EH had HEL values of 13.6 and 13.9 GPa, respectively, with a target thickness of 6.4 mm. At similar impact stresses with a target thickness of 9.9 mm, RH and EH had HELs of 13.9 and 13.1 GPa, respectively. The decreasing HEL results with increased target thickness for the EH could be described as precursor decay. However, it has been found that there is little precursor decay in ceramics. The trend in the RH HEL with thickness cannot be explained. Either it was material variability or the error associated with testing. If averages were taken of the HEL values, the HEL for RH would be 13.8 GPa and EH would be 13.5 GPa. There appears to be very little difference in HEL values between RH and EH.

4.3 Comparison to Other SiCs

The threshold for the spall values occurs at slightly higher impact stresses in the Hexoloy materials than that found for Sohio, FrS, and SiC-B. The Hexoloy thresholds occur around 5–7 GPa and the Dandekar (20) materials around 3–5 GPa. The Hexoloy appears to have spall values similar to the Sohio material (figure 34). At lower impact stresses, the Hexoloy has higher spall stresses than the FrS material; at the highest impact stress the spall strengths are similar. The HEL value for EH and RH were similar to that found by Bourne (25) for his sintered SiC.

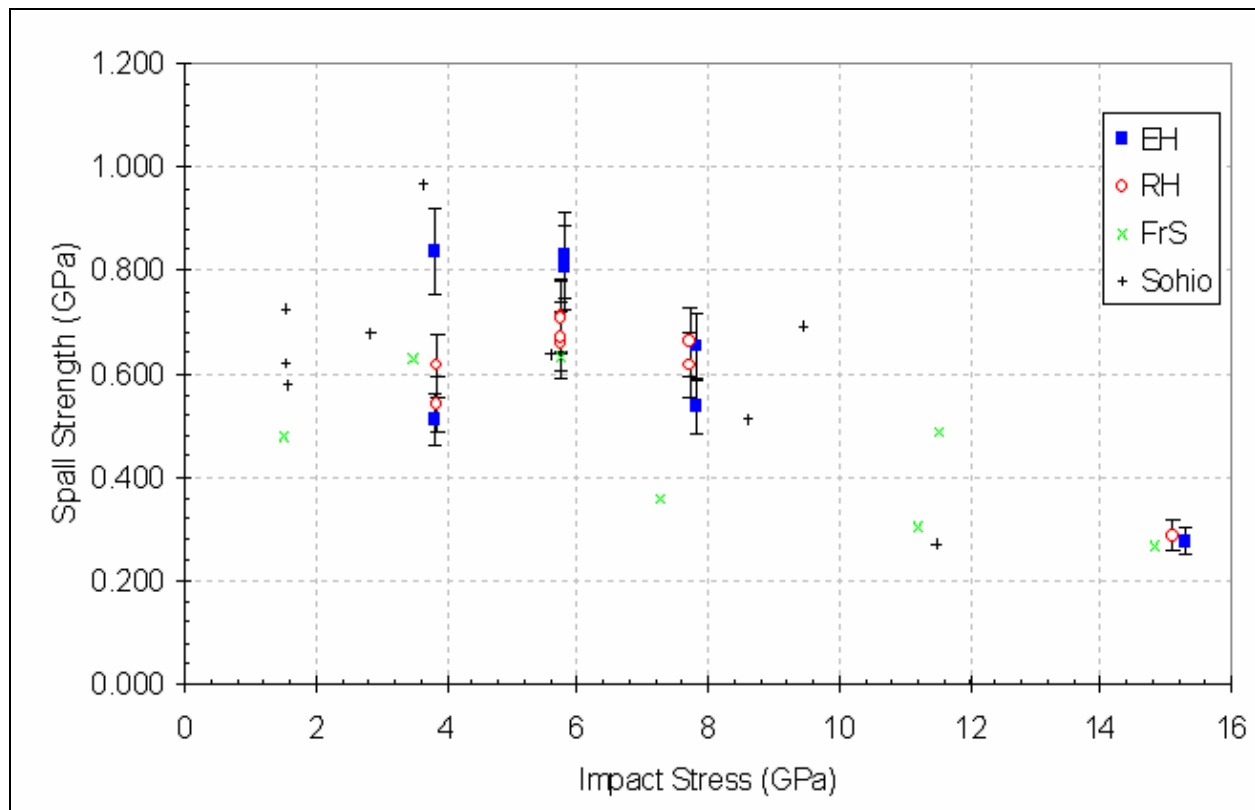


Figure 34. Comparison to other SiCs.

5. Conclusions

RH and EH obtained from Saint-Gobain were characterized microstructurally prior to plate-impact testing. Characterization included morphology, density, elastic wave speeds, hardness, fracture toughness, and flexure strength. Results showed RH and EH to be nearly identical except for differences in porosity distribution and flexure strength. RH samples had larger and a higher number of larger-sized pores. These act as large flaws and effectively lower the flexure strength of RH. EH samples had a flexure strength that was 18% higher than the RH samples. Plate-impact experiments were conducted to examine the influence of porosity distributions on the HEL and spall strengths of these two materials. Spall-strength experiments were conducted at different impact stresses and varying pulse widths. Stresses ranged from 3.8 to 15.3 GPa and pulse widths were 340 and 670 ns.

Results of these plate-impact experiments showed that, within the variability of the experimental results, there was no discernable difference between the spall strength values for RH and EH within the range of impact stresses and comparable pulse widths. To test for repeatability of the spall-strength results, one impact condition was repeated. The three experiments on RH at an impact stress of 5.8 GPa, with a pulse width of 340 ns, show spall-strength results within 8% of each other. The spall strengths showed a similar trend as observed by Dandekar and Bartkowski (18, 20, 26) with respect to impact stress. In SiC, spall strengths increase with impact stress to a threshold value and then decline. The threshold value for RH and EH appears to be between 5 and 7 GPa. Both materials show finite spall strengths above the respective HEL. The HEL values for RH and EH samples were 13.8 ± 0.2 GPa and 13.5 ± 0.6 GPa, respectively.

Despite the effect the large pores had on the quasi-static flexure strength levels between RH and EH, they had little influence on the dynamic behaviors. The triaxial stresses associated with uniaxial strain conditions seen in the plate-impact tests did not allow the bigger pores in RH to effect spall strength or HEL. The triaxial stress state confines the formation of large cracks from larger pores. Without the release in stress from the large cracks, a greater number of smaller pores and flaws affect material dynamic behavior. In contrast, the uniaxial stress conditions imposed by the four-point bend strength tests allow the initiation and propagation of large cracks from the large pores in RH.

In addition to the triaxial stress state, another possible reason for lack of difference between the spall strength values between RH and EH could be the result of the compressive wave that passes through the target prior to spallation. The damage caused by the compressive loading could be more severe than the damage caused by the large pores. This would result in similar spall strength values between the two material varieties.

The spall-strength results of the Hexoloys were comparable to the other sintered materials tested by Dandekar and Bartkowski (18, 20, 26). All the sintered materials had lower spall strengths than the hot-pressed varieties. This could be due to the higher density in the hot-pressed materials, the lower amounts of impurities present, or a combination of the two. Hot-pressed ceramics require less sintering aids. The HEL of the Hexoloys was comparable to that measured by Bourne (25) for his sintered SiC.

6. References

1. Hauver, G. E., et al. Enhanced Ballistic Performance of Ceramic Targets. Proceedings of the 19th Army Science Conference, USA, 1994.
2. Lundberg, P.; Renstrom, R.; Lundberg, B. Impact of Metallic Projectiles on Ceramic Targets: Transition Between Interface Defeat and Penetration. *International Journal of Impact Engineering* 2000, 24, 259–275.
3. Grady, D. E. Shock-Wave Compression of Brittle Solids. *Mechanics of Materials* 1998, 29, 181–203.
4. Grady, D. E. Shock-Wave Strength Properties of Boron Carbide and Silicon Carbide. *Journal de Physique IV* 1994, 4 (September 1994), C8-385–C8-391.
5. Orphal, D. L.; Franzen, R. R. Penetration of Confined Silicon Carbide Targets by Tungsten Long Rods From 1.5 to 4.6 km/s. *International Journal of Impact Engineering* 1997, 19 (1), 1–13.
6. Orphal, D. L., et al. Penetration of Confined Boron Carbide Targets by Tungsten Long Rods at Impact Velocities From 1.5 to 5.0 km/s. *International Journal of Impact Engineering* 1997, 19 (1), 15–29.
7. Orphal, D. L., et al. Penetration of Confined Aluminum Nitride Targets by Tungsten Long Rods at 1.5–4.5 km/s. *International Journal of Impact Engineering* 1996, 18 (4), 355–368.
8. ASTM B311. Test Method for Density Determination for Powder Metallurgy (P/M) Materials Containing Less Than Two Percent Porosity. *Annu. Book ASTM Stand.* 1997.
9. ASTM C1327. Standard Test Method for Vickers Indentation Hardness of Advanced Ceramics. *Annu. Book ASTM Stand.* 2003.
10. Moberlychan, W. J.; Cao, J. J.; De Jonghe, L. C. The Roles of Amorphous Grain Boundaries and the Beta-Alpha Transformation in Toughening SiC. *Acta Materialia* **1998**, 46 (5), 1625–1635.
11. Lee, W. E.; Rainforth, M. W. *Chapter 7: Synthetic Structural Non-Oxides*. In *Ceramic Microstructures Property Control By Processing*; Chapman & Hall: London, U.K., 1994; pp 415–432.
12. ASTM C1421. Standard Test Methods for Determination of Fracture Toughness of Advanced Ceramics at Ambient Temperatures. *Annu. Book ASTM Stand.* **2001**.
13. ASTM C1161. Standard Test Method for Flexural Strength of Advanced Ceramics at Ambient Temperature. *Annu. Book ASTM Stand.* **2002**.

14. Quinn, G. D.; Salem, J. A. Effect of Lateral Cracks on Fracture Toughness Determined by the Surface-Crack-in-Flexure Method. *Journal of the American Ceramic Society* **2002**, 85 (4), 873–879.
15. Barker, L. M.; Hollenbach, R. E. Laser Interferometer for Measuring High Velocities of Any Reflecting Surface. *Journal of Applied Physics* **1972**, 43 (11), 4669–4675.
16. Grady, D. E. Shock-Wave Properties of High-Strength Ceramics. In *Shock Compression of Condensed Matter*; Elsevier Science: New York, 1991.
17. Bourne, N., et al. The Effect of Microstructural Variations Upon the Dynamic Compressive and Tensile Strengths of Aluminas. *Proc. R. Soc. Lond. A* **1994**, 446, 309–318.
18. Dandekar, D. P.; Bartkowski, P. *Tensile Strengths of Silicon Carbide (SiC) Under Shock Loading*; ARL-TR-2430, U.S. Army Research Laboratory: Aberdeen Proving Ground, MD, 2001, p 38.
19. Dandekar, D. P. Spall Strength of Silicon Carbide Under Normal and Simultaneous Compression-Shear Shock Wave Loading. *International Journal of Applied Ceramic Technology* **2004**, 1 (3), submitted for publication.
20. Dandekar, D. P.; Bartkowski, P. Spall Strengths of Silicon Carbides Under Shock Loading. In *Fundamental Issues and Applications of Shock-Wave and High Strain-Rate Phenomena*; Staudhammer, K. P.; Murr, L. E.; Meyers, M. A., Eds.; Elsevier Science Ltd.: New York, 2001; pp 71–77.
21. Taylor, J. R. *An Introduction to Error Analysis*, 2nd ed.; University Science Books, 1996.
22. Dandekar, D. P.; Grady, D. E. Shock Equation of State and Dynamic Strength of Tungsten Carbide. In *Shock Compression of Condensed Matter-2001*; American Institute of Physics, 2002.
23. Feng, R.; Raiser, G. F.; Gupta, Y. M. Material Strength and Inelastic Deformation of Silicon Carbide Under Shock Wave Compression. *Journal of Applied Physics* **1998**, 83 (1), 79–86.
24. Grady, D. E. Shock Profile Studies on Selected Silicon Carbide Ceramics With Application to Dynamic Yield Mechanisms. In *Shock Compression of Condensed Matter-1999*; American Institute of Physics, 2000; pp 629–632.
25. Bourne, N.; Millett, J.; Pickup, I. Delayed Failure in Shocked Silicon Carbide. *Journal of Applied Physics* **1997**, 81(9), 6019–6023.
26. Bartkowski, P.; Dandekar, D. P. Spall Strengths of Sintered and Hot Pressed Silicon Carbide. In *Shock Compression of Condensed Matter-1995*; American Institute of Physics, 1996.

INTENTIONALLY LEFT BLANK.

Appendix: Specimen Preparation

A.1 Sectioning

Make sure sample is square and securely held in diamond saw. For SiC, use a diamond blade speed of 2500 rpm and a federate of 0.5 in/min.

A.2 Polishing

First, set samples in Bakelite. Then follow the process in table A-1 for polishing SiC using the automated polisher.

Table A-1. Polishing procedure for SiC.

Force (N)	Time (min)	Size Abrasive (μm)	Abrasive Type	Wheel/Holder Spin	Wheel speed (rpm)
15	3	45	Diamond film	Opposite	150
15	3	30	Diamond film	Opposite	150
30	4	15	Diamond slurry	Opposite	150
30	4	6	Diamond slurry	Opposite	150
30	8	1	Diamond slurry	Opposite	150
30	8	Colloidal silica	Diamond slurry	Opposite	150

A.3 Etching

Polished samples must be taken out of Bakelite before etching. Use a modified-murakami solution to etch the SiC samples.

A.4 Ingredients

- 20g NaOH
- 20g $K_3Fe(CN)_6$
- 50mL H_2O

Set up a stand in a hood and wearing the appropriate safety equipment, weigh and then mix the ingredients together in a Pyrex beaker. Boil for ~10 min.

A.5 Lapping and Polishing (ARL)

The 9.9-mm-thick plate-impact specimens were prepared at ARL. Precut cylindrical specimens were lapped on a Lapmaster machine using 500-grit SiC particles. Once the faces of the specimen were lapped flat, the probe side was manually polished on a polishing wheel. The process is described in table A.2.

Table A-2. Preparation of plate-impact specimens.

Abrasive Size (μm)	Abrasive Type	Polishing Cloth	Approx. Time (min)	Apparatus
~26 (500 grit)	SiC particles	—	—	Lapping machine
15	Diamond slurry	Texmet P	5	Polishing wheel
3	Diamond slurry	Texmet P	5	Polishing wheel
1	Diamond slurry	Texmet 2000	5	Polishing wheel

NO. OF
COPIES ORGANIZATION

1 DEFENSE TECHNICAL
(PDF INFORMATION CTR
ONLY) DTIC OCA
8725 JOHN J KINGMAN RD
STE 0944
FORT BELVOIR VA 22060-6218

1 US ARMY RSRCH DEV &
ENGRG CMD
SYSTEMS OF SYSTEMS
INTEGRATION
AMSRD SS T
6000 6TH ST STE 100
FORT BELVOIR VA 22060-5608

1 INST FOR ADVNCD TCHNLGY
THE UNIV OF TEXAS
AT AUSTIN
3925 W BRAKER LN STE 400
AUSTIN TX 78759-5316

1 US MILITARY ACADEMY
MATH SCI CTR EXCELLENCE
MADN MATH
THAYER HALL
WEST POINT NY 10996-1786

1 DIRECTOR
US ARMY RESEARCH LAB
IMNE AD IM DR
2800 POWDER MILL RD
ADELPHI MD 20783-1197

3 DIRECTOR
US ARMY RESEARCH LAB
AMSRD ARL CI OK TL
2800 POWDER MILL RD
ADELPHI MD 20783-1197

3 DIRECTOR
US ARMY RESEARCH LAB
AMSRD ARL CS IS T
2800 POWDER MILL RD
ADELPHI MD 20783-1197

NO. OF
COPIES ORGANIZATION

ABERDEEN PROVING GROUND

1 DIR USARL
AMSRD ARL CI OK TP (BLDG 4600)

NO. OF
COPIES ORGANIZATION

1	COMMANDER US ARMY TACOM PM COMBAT SYSTEMS SFAE GCS CS 6501 ELEVEN MILE RD WARREN MI 48397-5000
1	COMMANDER US ARMY TACOM AMSTA SF WARREN MI 48397-5000
1	COMMANDER US ARMY TACOM PM SURVIVABLE SYSTEMS SFAE GCSS W GSI H M RYZYI 6501 ELEVEN MILE RD WARREN MI 48397-5000
1	COMMANDER US ARMY TACOM CHIEF ABRAMS TESTING SFAE GCSS W AB QT T KRASKIEWICZ 6501 ELEVEN MILE RD WARREN MI 48397-5000
13	COMMANDER US ARMY TACOM AMSTA TR R R MCCLELLAND D THOMAS J BENNETT D HANSEN AMSTA JSK S GOODMAN R SIERS D TEMPLETON A SCHUMACHER AMSTA TR D D OSTBERG L HINOJOSA B RAJU AMSTA CS SF H HUTCHINSON F SHWARZ WARREN MI 48397-5000
1	SURVICE ENGINEERING COMPANY B BRUCHEY 4695 MILLENIUM DRIVE BELCAMP MD 21017-1505

NO. OF
COPIES ORGANIZATION

ABERDEEN PROVING GROUND

61	DIR USARL AMSRD ARL WM T WRIGHT J MCCAULEY AMSRD ARL WM MD B CHEESEMAN E CHIN P DEHMER R DOOLEY G GAZONAS S GHIORSE M KLUSEWITZ J LASALVIA W ROY J SANDS D SPAGNUOLO S WALSH S WOLF AMSRD ARL WM TA P BARTKOWSKI M BURKINS R DONEY W GILLICH B GOOCH T HAVEL E HORWATH T JONES P KINGMAN D KLEPONIS B LEAVY I LSKO S MARTIN (15 CPS) M NORMANDIA W ROWE J RUNYEON K STOFFEL M ZOLTOSKI AMSRD ARL WM TB P BAKER AMSRD ARL WM TD T BJERKE D CASEM J CLAYTON D DANDEKAR K IYER B MEYER M RAFTENBERG E RAPACKI S SCHOENFELD T WEERASOORIYA
----	---

NO. OF
COPIES ORGANIZATION

AMSRD ARL WM TE
A NILER
J POWELL
AMSRD ARL WM MB
J SWAB